Improved Equatorial Upper Ocean Vertical Mixing in the NOAA/GFDL OM4 Model

Brandon G. Reichl[1]*, Andrew T. Wittenberg[1], Stephen M. Griffies[1,2], Alistair J. Adcroft[2]

[1]NOAA Geophysical Fluid Dynamics Laboratory, Princeton, NJ, USA
[2]Princeton University Program in Atmospheric and Oceanic Science, Princeton, NJ, USA

Key Points:

- Large eddy simulation results are used to evaluate the diurnal cycle of equatorial turbulent mixing in the OM4 ocean and sea-ice model.
- Too strong background viscosity in an ocean model can reduce shear in the equatorial undercurrent and degrade its induced vertical mixing.
- Vertical grid spacing of a few meters helps resolve shear mixing events within and below the equatorial undercurrent in ocean models.

*Princeton, NJ

Corresponding author: Brandon G. Reichl, brandon.reichl@noaa.gov

Abstract

Deficiencies in upper ocean vertical mixing parameterizations contribute to tropical upper ocean biases in global coupled general circulation models, affecting their simulated ocean heat uptake and ENSO variability. To better understand these deficiencies, we develop a suite of ocean model experiments including both idealized single column models and realistic global simulations. The vertical mixing parameterizations are first evaluated using large eddy simulations as a baseline to assess uncertainties and evaluate their implied turbulent mixing. Global models are then developed following NOAA/GFDL's 0.25° nominal ocean horizontal grid spacing OM4 (uncoupled ocean) configuration of the MOM6 ocean model, with various modifications that target improvements to biases in the original model. We identify a variety of enhancements to the existing mixing schemes that are evaluated using observational constraints from TAO moorings and Argo floats. In particular, we find that we can improve the diurnal variability of mixing in OM4 via modifications to its mixing scheme, and that we can improve the net mixing in the upper thermocline by reducing the background vertical viscosity, allowing for more realistic, less diffuse currents. The improved OM4 model better represents the mixing and its diurnal deep-cycle variability, leading to more realistic time-mean tropical thermocline structure, mixed layer depths, SSTs, and a better Pacific Equatorial Undercurrent.

Plain Language Summary

Computational models of oceanic and atmospheric circulation are a critical tool for understanding and projecting the Earth's climate. These models have errors that can arise due to many potential sources, including model formulation or the choices in applying the model. One of the more well known sources of error is the representation of turbulent mixing processes. In this work we consider specially designed small-scale models that simulate turbulent mixing and use their results to improve the representation of turbulence and its induced mixing in large-scale models. In particular, we investigate how the intensity of mixing varies over the day, considering the progression from cooler nighttime conditions to strong heating from the sun during the day. We find some modifications to the mixing scheme in the ocean climate model that can improve the model solutions when compared to the real ocean.

1 Introduction

Coupled atmosphere-ocean general circulation models (CGCMs) are crucial tools for understanding and projecting the Earth's climate system and its response to changing climate forcings (IPCC, 2021). However, these models remain imperfect due to several factors, including their often coarse lateral and vertical resolution (to support timely production of seasonal forecasts and centennial projections) and incomplete parameterizations of unresolved physical processes (e.g. Palmer et al., 2005; Hawkins & Sutton, 2009). Improving confidence in these models requires efforts on many fronts, and in this work we focus on the representation of upper ocean vertical mixing in the ocean general circulation model (OGCM) component of these CGCMs.

Vertical mixing in the upper ocean is particularly important for CGCMs, due to its role in mediating the exchange of mechanical energy, thermal energy, and other tracers (e.g., chemical compounds) between the atmosphere and ocean interior. Vertical mixing also strongly influences rapid (e.g., diurnal to subseasonal) air-sea coupled processes, as properties are most efficiently mixed between the atmosphere and ocean turbulent boundary layers. At these time scales, the depth of the ocean surface boundary layer sets both the effective heat and chemical capacity of the ocean, and the inertial resistance of near-surface currents to acceleration by surface wind stresses.

Ocean mixing processes in the tropical oceans play a key climate role, since large scale atmosphere-ocean coupled interactions occur in this region and affect the global heat balance and meridional temperature and precipitation patterns. A quintessential example of a coupled interaction is the El Niño / Southern Oscillation (ENSO) phenomenon (McPhaden et al., 2020), which is characterized by basin-scale changes in equatorial sea surface temperature (SST), trade winds, currents, and patterns of upper ocean heat content. ENSO is one of the most important modulators of global climate patterns, through its various teleconnections (e.g. Ropelewski & Halpert, 1987; Trenberth et al., 1998; L'Heureux et al., 2015; X. Li et al., 2021). Simulating a realistic ENSO in a CGCM requires skill in simulating many relevant ocean and atmosphere processes, as well as the processes that govern the air-sea interface exchange . It is therefore hypothesized that deficiencies in upper ocean mixing of CGCMs can degrade not only the simulated local ocean and atmosphere state, but also the simulated global climate, climate variability, and climate response of the model (Meehl et al., 2001; Richards et al., 2009).

One of the common tropical upper ocean CGCM biases in the tropics is an overly strong and westward-shifted equatorial Pacific cold tongue (G. Li & Xie, 2014), which interacts with other biases in the CGCM. The CGCM's predicted ocean SST near the equator is tightly connected to the strength, position, and watermass properties of its thermocline (G. Li & Xie, 2012), which results from a balance of atmospheric forcing, ocean vertical mixing physics, and resolved and parameterized horizontal advection. Atmospheric forcing directly affects the SST through its impact on surface heat and freshwater fluxes and radiation (e.g., via clouds, evaporation, and the diurnal cycle of shortwave radiation). The simulated winds also modulate the depth of the thermocline due to the Ekman pumping effects associated with the wind stress curl (Kessler, 2006; Chiodi & Harrison, 2017; Voldoire et al., 2019) and through transient adjustments via oceanic internal Rossby and Kelvin waves. The ocean vertical mixing processes also play a key role in setting the SST and sea surface salinity (Farneti et al., 2022) by setting the vertical gradients of temperature, salinity, and density above the thermocline.

Numerous experiments have sought to characterize upper ocean turbulence near the equator, starting with observational efforts documented by Gregg et al. (1985) and Moum and Caldwell (1985) and followed with high-resolution numerical large eddy simulation (LES) studies (Wang et al., 1996, 1998; Pham et al., 2013; Whitt et al., 2022). Upper ocean vertical mixing near the equator modulates SST on timescales ranging from diurnal to seasonal (Moum et al., 2013) and supports time-mean subsurface downward heat fluxes that may exceed 200 W/m^2 at ~ 100 m depth close to the equator. The turbulence that drives this mixing is primarily energized by current shear instability mechanisms (Peters et al., 1994; C. Sun et al., 1998; Moum et al., 2011; Smyth & Moum, 2013), with those currents including both time-mean and transient contributions from the local wind driven flow, tropical instability waves, equatorial Kelvin waves, and basin-scale subsurface undercurrents such as the Equatorial Undercurrent (Holmes & Thomas, 2015; Cherian et al., 2021). The presence of a strong diurnal cycle of surface heating in the tropics strongly modulates the water column stability, driving a diurnal response in turbulence and mixing referred to as deep-cycle turbulence (Smyth & Moum, 2013).

As a primarily shear-driven turbulence, the potential for instability due to the mean flow is often characterized using the gradient Richardson number that relates the competition between stabilizing buoyancy frequency ($N^2 = -g\rho^{-1}\partial_z\rho$, where g is gravity, and ρ is *in situ* density that depends on temperature, salinity, and local pressure) and destabilizing shear frequency ($S^2 = (\partial_z u)^2 + (\partial_z v)^2$, where u and v are the zonal and meridional components of the current):

$$Ri = \frac{N^2}{S^2} = \frac{-g\partial_z(\rho)}{\rho\left((\partial_z u)^2 + (\partial_z v)^2\right)}. \tag{1}$$

Observational campaigns have documented a diurnal variation of Ri that indicates the presence of marginally stable water (e.g., Ri slightly greater than 0.25) from the near surface down to the thermocline during the day, that is rapidly destabilized ($Ri < 0.25$) at night (e.g. Smyth & Moum, 2013). At night, this downward destabilization is fed by a downward flux of shear that propagates turbulence, momentum, and heat from the warm surface layer to cooler waters at depth, consistently approaching 100 m at 140°W (Smyth et al., 2013). These same patterns have been observed in long term turbulence measurements in both the Pacific and Atlantic basins (Moum et al., 2022), and likely also occur in the Indian Ocean (Pujiana et al., 2018).

While the characteristics of this turbulence are now fairly well known from observations and process models, the connection to the mean flow and turbulent fluxes in CGCMs requires accurate turbulence closure parameterizations to properly capture the spatiotemporal patterns and state-dependence (see Pei et al., 2020). Approaches to parameterize upper ocean turbulence vary among different OGCMs, where it is relatively common to employ bulk models for the boundary layer that are coupled to interior shear mixing schemes below (Large et al., 1994; Reichl & Hallberg, 2018). Comparing the various bulk approaches with one or two-equation turbulent kinetic energy (TKE) based schemes confirms that there is significant uncertainty remaining in representing ocean vertical mixing processes in ocean models (Q. Li et al., 2019). A key part of resolving this uncertainty is careful evaluation of various mixing schemes against high-fidelity LES, which is one goal of this study. A further complication is the expectation that very fine vertical resolution in an ocean model may be required to achieve optimal performance from a given vertical mixing scheme (Jia et al., 2021), with this expectation also examined in this work.

In this study we focus on the application of parameterized upper ocean mixing processes in the ocean component of a recent-generation CGCM (e.g., part of the Coupled Model Intercomparison Project 6, or CMIP6 era, see Eyring et al. (2016)) to represent tropical mixing patterns and stratification, and in particular investigate the impact of improved mixing on biases in the ocean mean state and variability. Although our ultimate goal is to improve the representation of upper ocean stratification and circulation via ocean mixing in CGCMs, our first step is to investigate the sensitivity of the ocean component to changes in mixing under atmospheric forcing arising from a prescribed atmospheric state. In Section 2 we describe the ocean configuration, namely the NOAA Geophysical Fluid Dynamics Laboratories Ocean Model 4 (OM4, Adcroft et al., 2019), and discuss the key upper ocean physics parameterizations used within OM4 that are investigated in this work. In Section 3 we utilize a recent LES study of turbulence near the equator at 140°W (Whitt et al., 2022), to evaluate the turbulent fluxes predicted by OM4 in a one-dimensional column model configuration. In Section 4 we follow the LES exercise by analyzing several additional changes required in OM4 to improve the simulated tropical currents and stratification. We conclude with a summary and future outlook for improved mixing schemes in CGCMs.

2 OM4 and Baseline Evaluation

Forced OGCM simulations, where the atmospheric fields are not interactive (e.g., following the 2nd Ocean Model Intercomparison Protocol OMIP2, Griffies et al., 2016; Tsujino et al., 2020), provide an approach to assess ocean model biases in a simpler context than CGCMs. The reason we employ this approach is partially to simplify the analysis by avoiding the complex coupled feedbacks and chaotic variability that occur in CGCMs (which require long runs or large ensembles to sample adequately). We also assume that since the winds in the reanalysis products are constrained by observations, they should be closer to nature than those from CGCMs. This assumption may be somewhat flawed, since the reanalyses used to drive OMIP style simulations contain their own biases (Taboada et al., 2019), which contribute to specific circulation biases in the tropics (e.g. Z. Sun et al., 2019). Further complicating the use of OMIP runs to assess ocean sensitivities is that the ocean biases may not have the same magnitude or even sign as in the CGCM (see Adcroft et al., 2019, also demonstrated later in this section). Despite these cautions, current generation forcing datasets, such as the JRA55-do product developed during OMIP2 (Tsujino et al., 2018), represent a practical first step to produce realistic ocean simulations for comparisons over the recent historical epoch.

The base OMIP2 simulations studied here use NOAA Geophysical Fluid Dynamics Laboratory's (GFDL) OM4 ocean and sea-ice model (Adcroft et al., 2019), which is a coupled configuration of the Modular Ocean Model 6 (MOM6) and Sea Ice Simulator 2 (SIS2) code bases. OM4 is used as the ocean and sea-ice components of GFDL's CM4 CGCM (Held et al., 2019), thus the improvements investigated here can readily inform future climate model development. OM4 also closely resembles the ocean and sea-ice component of GFDL's ESM4.1 CGCM (Dunne et al., 2020) and the Seamless System for Prediction and Earth System Research (SPEAR, Delworth et al., 2020), such that improvements to ocean mixing physics should also benefit other coupled modeling efforts. Unless otherwise noted, we follow the same approach as OM4 for our main configuration choices, including a nominally 0.25° tripolar horizontal grid and hybrid z^* (stretched geopotential) and σ_2 (potential density referenced to 2000 dbar) vertical coordinate (e.g., OM4p25, see Adcroft et al., 2019). We update the forcing to use the most recent JRA55-do reanalysis product (version 1.5), which is an update from Tsujino et al. (2018) including some bugfixes and additional years (we present results through the end of 2018). The JRA55-do forcing provides lower atmosphere values needed for computing air-sea fluxes, including the near surface temperature, humidity, pressure, and winds at 3 hour intervals with a horizontal spacing of $\approx 0.5°$. The JRA55-do forcing also provides longwave and shortwave heat fluxes as well as freshwater fluxes at similar intervals. We employ the same sea surface salinity restoring to climatology as Adcroft et al. (2019), with the restoring piston velocity set to 0.1667 m/day.

There are numerous ocean physics parameterizations within MOM6 that are used by OM4, which play significant roles in its simulated ocean currents and hydrography in the top several hundred meters of the tropical oceans. In the next subsection we describe only the most relevant parameterizations, focusing on those examined in this study. For a complete description of OM4 see Adcroft et al. (2019).

2.1 OM4 physical configuration

The ocean surface boundary layer is a particularly important region of vertical mixing, which is often represented in ocean models using combinations of parameterizations for different physical processes. Vertical fluxes in OM4's ocean surface boundary layer are provided via eddy mixing coefficients from the ePBL (energetic Planetary Boundary Layer) mixing parameterization (Reichl & Hallberg, 2018). These ePBL mixing coefficients are supplemented by an interior stratified shear mixing scheme, which follows the TKE-diffusivity mixing scheme described in Jackson et al. (2008, hereafter JHL). The vertical mixing predicted in OM4 by ePBL and JHL is tested in detail in this study using LES reference simulations in section 3, resulting in a proposed mixing formulation that improves biases relative to the OM4 configuration. The vertically homogenizing turbulent fluxes primarily originate from ePBL and JHL in the upper ocean, and are opposed by submesoscale mixed layer eddy (MLE) restratification, which is parameterized as described by Fox-Kemper et al. (2011).

Interior mixing in OM4 is also parameterized using several different schemes that represent effects of different physical processes. The interior background vertical diffusivity in OM4 is determined by the latitude, as motivated by internal wave properties and described in Harrison and Hallberg (2008), which yields a background vertical diffusivity of temperature and salinity increasing from 2×10^{-6} m^2 s^{-1} at the Equator to 1.15×10^{-5} m^2 s^{-1} at $\pm 60°$ latitude. The baseline background vertical viscosity is estimated from the vertical diffusivity by assuming a Prandtl number of 1.0, and supplemented with an additional constant background vertical viscosity of 10^{-4} m^2 s^{-1} everywhere. The effects of this additional constant background vertical viscosity, which results primarily from historical convention and is not linked to a specific physical process, are examined in section 4. Tropical ocean stratification is also sensitive to parameterized shortwave penetration (e.g. Gnanadesikan & Anderson, 2009). OM4 estimates shortwave penetration profiles using the optical model of Manizza (2005), together with a monthly chlorophyll climatology. Finally, horizontal eddy mixing of momentum is achieved with a biharmonic Smagorinsky lateral viscosity (Griffies & Hallberg, 2000); there is no additional parameterized lateral mixing of tracers.

2.2 Climatological OM4 Equatorial stratification bias

We now establish the baseline biases in OM4, here simulated using the OMIP2 protocol with the JRA55-do atmospheric state. We first examine the equatorial longitude-depth section of temperature and salinity, averaged from 1°S to 1°N (Figure 1). The observational product chosen for comparison is based on the updated (through 2022) Argo ocean state estimates (Roemmich & Gilson, 2009), though a similar comparison could be found with model based reanalysis products for the climatology (e.g. Chang et al., 2013). The SST in OM4 is generally warmer than observed in all equatorial basins (see panel 1e). Each basin also shows interior cold biases linked to vertical displacements of the thermocline, though a notable interbasin difference is that the bulk of the interior (e.g., 500 m to 100 m) is warm in the Indian but cold in the Pacific and Atlantic. OM4 is saltier than the Argo climatology at the surface, except near the Maritime Continent (see panel 1f). Unlike the Indian Ocean basin, which shows salty biases below 100 m, the Atlantic and Pacific show fresh biases below 100–200 m depth.

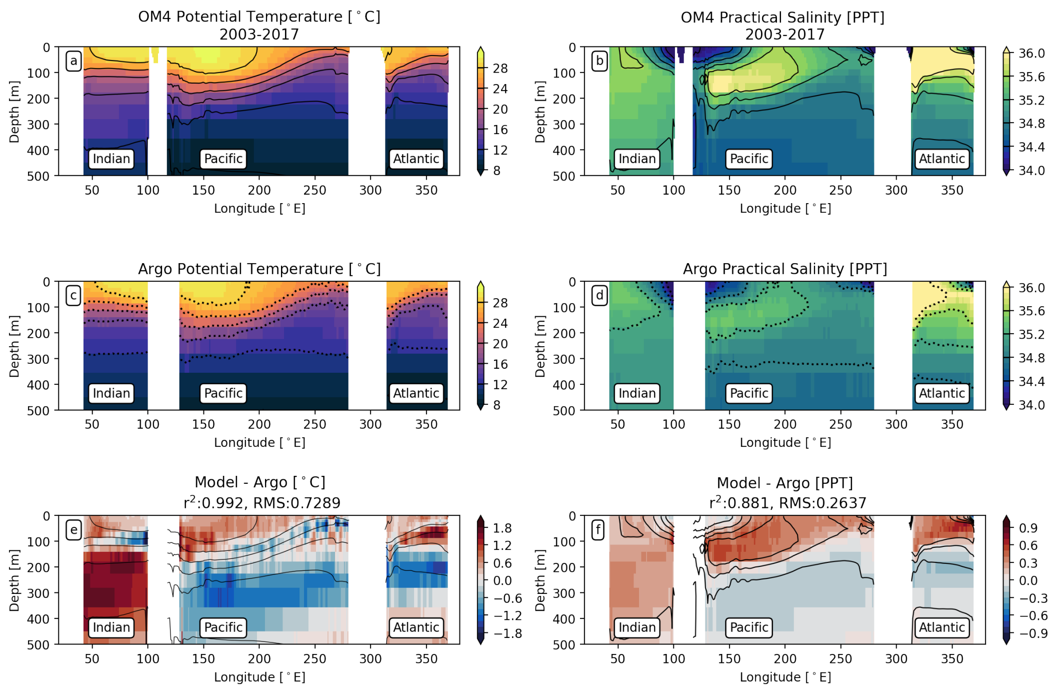

Figure 1. OM4 climatological potential temperature (panel a) and practical salinity (panel b), similar from (Roemmich & Gilson, 2009) Argo climatology (panels c and d, 2004-2020), and the respective differences (OM4 minus Argo, panels e and f), all averaged from 1° S to 1° N. The panel titles for the bias maps include the r^2 (Pearson correlation coefficient squared) and RMS (square root of the mean square difference) difference metrics. For the climatology maps, the contour intervals are mapped via interpolation at every fourth pcolormesh interval, as indicated on the colorbars. The model contours are repeated in the difference maps to facilitate comparison.

The corresponding biases in thermal and haline vertical stratification ($\partial_z\theta$ and $\partial_z S$) also show dependence on depth and basin (Figure 2). The Indian ocean basin again looks distinct from the Pacific and Atlantic Ocean basins. The biases in the Indian basin are mainly a strong temperature stratification between 50-100 m and weak temperature stratification between 100-150 m, roughly corresponding to a shoaling of the equatorial thermocline (see panel 2e). The Pacific and Atlantic basins show generally high stratification bias (e.g., red shading) in the upper 300m, with a layer of lower stratification (e.g., blue shading) likely indicating that the thermocline is too strong in its upper part and is shifted to be overly shallow in OM4 compared to observational product. The salinity stratification is also strong in the model, with excessive negative $\partial_z S$ near the surface in the western Atlantic and Pacific basins, above regions of excessive positive $\partial_z S$ (see panel 2f). These stratification biases suggest that there may be too little mixing by ePBL/JHL (or too much restratification by MLE) in the upper ocean in OM4.

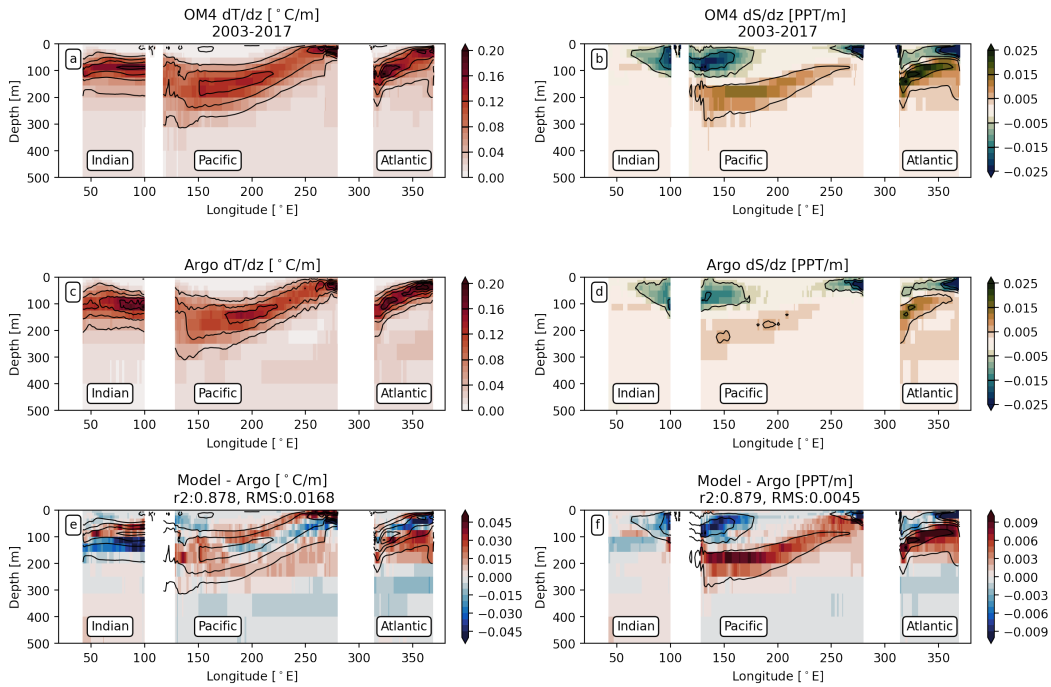

Figure 2. As in Figure 1, but for the vertical derivatives of temperature and salinity.

2.3 Relationships between OM4 and CM4 Tropical stratification biases

For reference to the CM4 CGCM counterpart to OM4, we briefly contrast the OM4 equatorial transect biases to the CM4 biases. The CM4 temperature and salinity differences from OM4 and their biases from Argo are shown in Figure 3 and similar maps for stratification are shown in Figure 4. As explained in Adcroft et al. (2019), OM4 and CM4 do not have the same sign SST bias at the equator (which remains true here with JRA55-do v1.5 forcing), and this difference can be seen to apply throughout the upper 500 m of these simulations. CM4 is significantly colder in the upper parts of all basins, though the warm Indian basin bias at depth is common to OM4 and CM4. Since the ocean component of these models is the same, these differences must be linked to differences in the ocean-atmosphere fluxes — arising from either the atmospheric model component, or its response to the OGCM-generated SSTs, or from subsequent coupled ocean-atmosphere interactions that can modify biases seeded by either component.

The stratification biases are significantly worse in CM4 relative to OM4, but generally show similar patterns suggesting that these are biases originating in OM4 and are less sensitive to the details of the surface forcing. In particular, the strong shallow stratification that plagues all three eastern equatorial basins, and the shoaling of the equatorial thermocline relative to observations, are similar between OM4 and CM4. Since stratification is directly impacted by vertical mixing, the common biases observed here between OM4 and CM4 suggest that the time-mean stratification could be a useful metric to evaluate the impact of ocean mixing parameterizations, which may yield relatively consistent impacts in both the OGCM and CGCM.

2.4 Variability of currents, current shear, and stratification in the equatorial Pacific

2.4.1 Observation based metrics from TAO stations

While the mean state biases are a useful bulk metric to analyze the OM4 and CM4 simulations relative to observation based fields, the tropics are characterized by significant variabil-

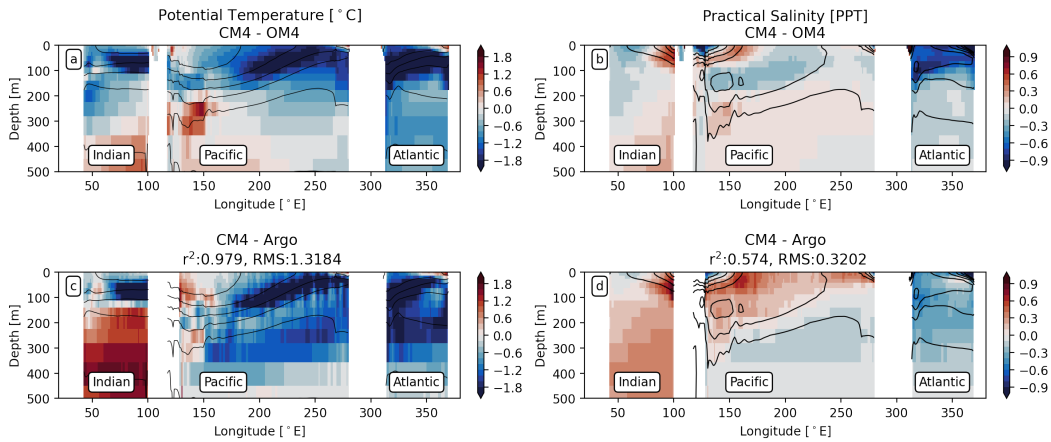

Figure 3. Difference of CM4 from OM4 for climatological potential temperature (panel a) and practical salinity (panel b) and the respective difference of CM4 minus Argo climatology (panels c and d), all averaged from 1° S to 1° N. The panel titles for the Argo bias maps include the r^2 (Pearson correlation coefficient squared) and RMS (square root of the mean square difference) difference metrics. The contour intervals in each panel are mapped from CM4 via interpolation at at the same intervals used in Figure 1 to facilitate comparison.

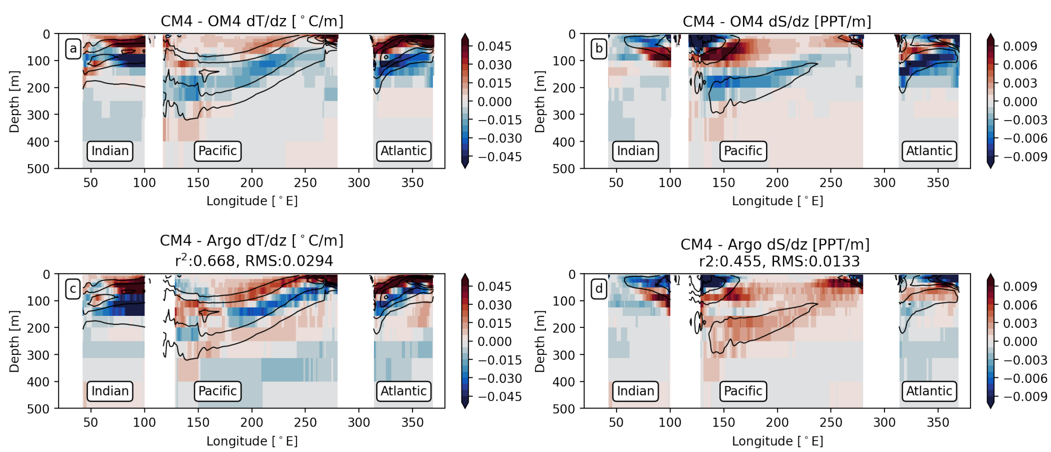

Figure 4. As in Figure 3, but for the vertical derivatives of temperature and salinity.

ity about this mean state on diurnal, weekly, seasonal, and interannual timescales. We therefore also desire some metrics to evaluate the ability of OM4 to reproduce the variability of these ocean properties. The long term, high-frequency nature of the observations taken along the Tropical Atmosphere Ocean (TAO) mooring array provides a useful database to assess these properties of the model. We therefore develop the additional method of comparing high-frequency profile outputs taken from OM4 runs to the four TAO moorings with long-term ADCP (acoustic Doppler current profiler) records across the equatorial Pacific basin (165° E, 170° W, 140° W, and 110° W). We focus on the time period from 2001-2008 in this analysis to facilitate comparison with similar model simulations in subsequent sections. Since we want to understand the variability of the various fields from the mean, we introduce a set of plots that map the percentile distribution of the current speed as a function of depth in the ADCP data (Figure 5, upper row). The heat maps in the figures map the percentile of the time series as a function of depth and zonal current speed. The value of the current speed at the 0.5 percentile value represents the median current profile, and by looking at the smaller and larger percentiles we map the envelope of the range of the observed current distribution at each depth. The range of observed currents is typically bounded between about -1 and 2 m s^{-1}, with significant variability at all locations and significant structure in the mean current profile. The heat maps also yield insight into the typical structure of the EUC, and its depth and strength as it flows from west to east.

Since the instability mechanisms driving the ocean mixing are governed by shear-driven instabilities, we also plot the percentile heat map for the squared zonal current shear of the ADCP observed currents (Figure 5, panels e-h). The shear yields a pattern that shows that typically the highest shear values occur above the mean position of the core of the EUC (e.g., the position of the peak positive values in the zonal current, u), with a kink indicating lower values of mean shear in and below the core of the EUC. The heat maps suggest considerable variability in the current shear, which may be related to large-scale current variability, meridional meanders of the EUC, and internal waves. The ADCP also provides the meridional component of the current, which can contribute to the total shear. Including the meridional currents in the shear would not qualitatively affect the results presented here or in subsequent sections of this study. The meridional currents are therefore neglected for this analysis because it would complicate our later comparison with the c-grid model currents (Arakawa & Lamb, 1977), where the OM4 grid is specified so that the zonal component of the currents are located on the equator.

The stratification cannot be accurately evaluated from the TAO buoys since the vertical spacing of temperature (and sometimes salinity) measurements often exceeds 10-20 m within the upper 200 m. We therefore take an alternative approach and diagnose stratification from individual Argo profiles from the Argo float database (Argo, 2023), which usually record temperature and salinity at a vertical spacing of roughly $1-4$ m. We locate all Argo profiles within ±0.5 degrees of the equator in latitude and within ±5 degrees of the station in longitude, where this aspect ratio allows us to obtain significantly more float matches and robust statistics, and is justified since the meridional scale of the EUC and thermocline variability is much smaller than its zonal scale (we also note a 1-2-1 binomial filter is applied to the profiles if the vertical spacing in pressure is less than 2 dbars to facilitate compositing data from varying vertical resolution). The stratification heat maps produced from the Argo profiles very clearly demonstrate significant statistical variations of the stratification about the thermocline (see Figure 5, panels i-l). It would be useful to analyze Ri directly from the TAO/Argo observations, but since the N^2 profiles are not precisely located with the TAO buoy we are not able to take that approach here.

2.4.2 Virtual stations in OM4 and comparison

To facilitate the comparison of the OM4 model output with the heat maps, we rerun the OM4 model, but with a few changes. First, we implement virtual buoys into the OM4 model that store model profile output at 2 hourly mean time sampling (the ADCP data is similarly time averaged). Second, we shift from the hybrid ($z_*-\sigma_2$) coordinate of the OM4 model to a $z*$ based coordinate, which is done to maintain specified vertical resolution (2 m telescoping spacing) in the upper ocean for computing vertical gradients. We note that the $z*$ based version of OM4 is expected to have significantly more spurious mixing than the hybrid coordinate model (Adcroft et al., 2019), which is an unfortunate trade-off deemed necessary due to the relatively poor vertical resolution in the original hybrid coordinate in the Western Pacific (we comment more on the concerns related to the vertical coordinate in the discussions section). Finally, the OM4 models with the high-resolution output are rerun only for the time period of 1999-2008 (the same time period focused on for the ADCP analysis), and we set aside the first two years of this integration as spin-up. We extended one OM4 simulation to 2022 and confirmed that the sampling through 2008 is sufficient to yield a robust statistical analysis.

The comparison between the percentile heat maps for currents, zonal shear, and stratification in OM4 and the observations are shown in Figure 6. The biases in the mean currents from OM4 are characterized as a shallow EUC core in the West that improves moving toward the East

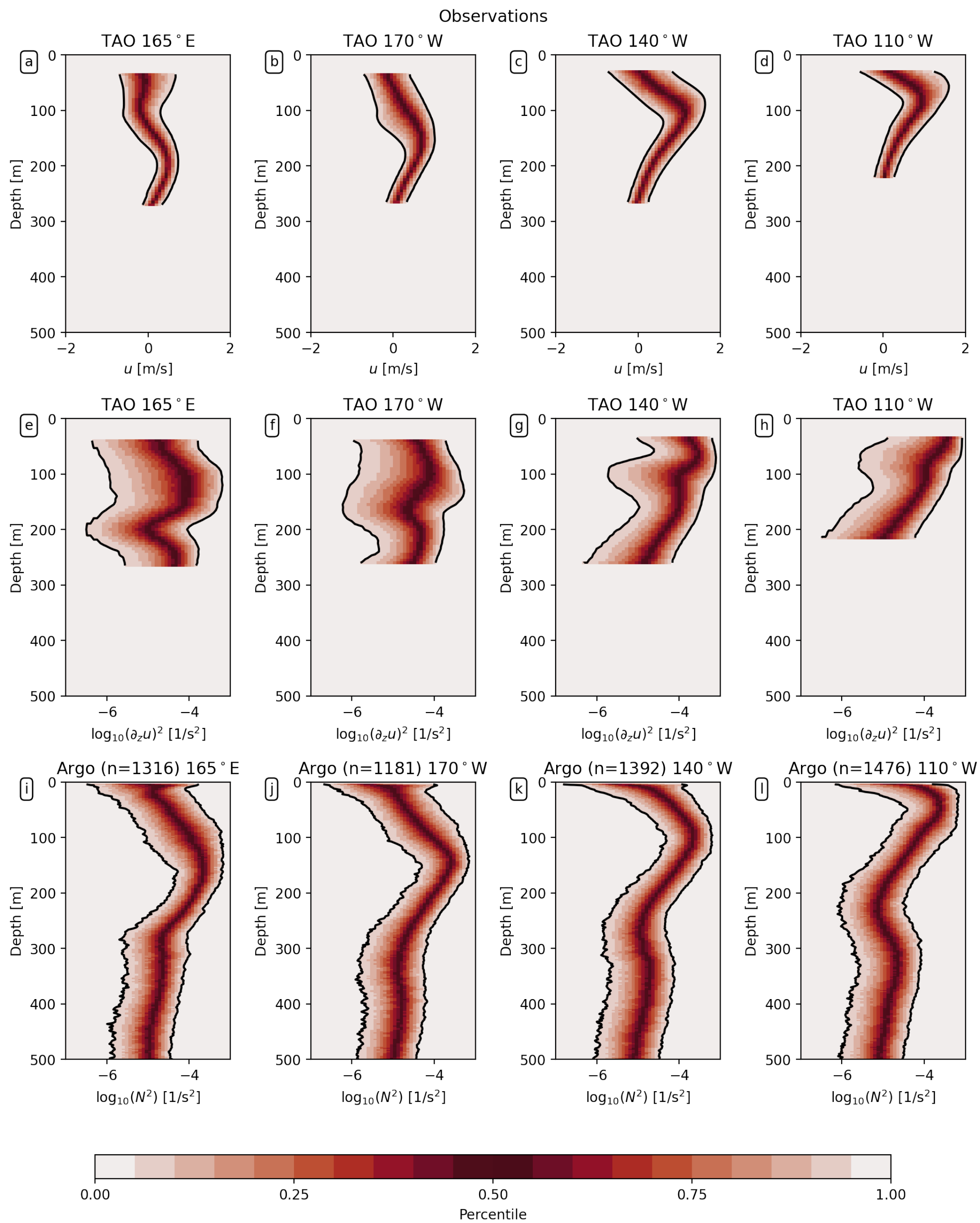

Figure 5. Percentile maps as a function of depth for the ADCP zonal current (upper row), zonal current shear (center row), and Argo derived stratification (bottom row). The columns represent four longitudes on the equator that host long term TAO buoy ADCP measurements. The solid lines in each panel trace the 5th and 95th percentile values. The TAO data covers the years from 2001-2008, while the Argo data includes the full Argo time period (through 2022) to increase the number of samples (indicated by n in each panel title).

(see panels 6a-d), with a reasonable range of variability compared to the observations (inferred by comparing the spacing between the 5th and 95th percentile traces). The biases in the shear indicate that the shears in OM4 tend to be too weak in the West below about 100 m, a bias that is consistent at each mooring moving towards the east. In the far east (e.g., 110° W), the shear in the model appears to reasonably well capture the values in the observations in terms of the minimum values, but again it underestimates the peak and maximum shear values below about 80 m. The stratification percentile heat maps are consistent with the results from the mean stratification bias maps, where OM4 tends to have too much stratification in shallower depths (e.g., between 10 m and 50 m). The median stratification comparisons below about 100 m look to be reasonable, though the models give a very narrow distribution of stratification compared to observations. The lack of variability in the model stratification may be largely associated with unresolved internal waves, though the model does capture more variability in terms of the current shears. In general these biases are consistent with the suggestion from the mean stratification that OM4 predicts too little overall mixing (or overpredicts restratification) in the range of about 20 m to about 100 m. We test this hypothesis in the next section with a more direct analysis of OM4's vertical mixing parameterizations using LES models.

3 Evaluating and adjusting upper ocean parameterizations in OM4: an LES approach

In-situ ocean observations of properties like temperature, salinity, and current speeds are the gold standard for evaluating numerical ocean models. However, directly testing ocean mixing schemes at the process level has traditionally been conducted using idealized, high resolution numerical models, especially LES. The reason for the popularity of the LES approach is largely due to the difficulties in untangling the role of multiple error sources in models from model biases. A recent process study by Whitt et al. (2022) presents a realistic pair of tropical LES in the region of interest for this study, which are thus chosen to assess the upper ocean mixing in the baseline OM4 model. In Whitt et al. (2022), these LES solutions were evaluated extensively in comparison to mooring estimated vertical turbulent heat fluxes.

This set of LES is formulated to resolve the one-dimensional (vertical) turbulent mixing processes that are parameterized in OGCMs like OM4. However, in the equatorial oceans the vertical mixing is significantly modulated by large-scale horizontal processes ($> 10^6$ m) that are not captured at the horizontal scales of the LES domain ($\leq 10^4$ m). In this set of experiments, the large-scale processes are therefore included by prescribing a time-varying profile of the time-tendencies of ocean currents, temperature, and salt into the LES equations. These tendencies are extracted from the output of a separate three-dimensional regional model that spans the equatorial Pacific domain (see Whitt et al., 2022). To facilitate a comparison between OM4's vertical mixing and the LES, we therefore implement the capability in MOM6 to read the same external forcing time-tendency terms for temperature, salinity, and momentum, following Whitt et al. (2022). This method allows the one-dimensional (column) version of OM4 to represent the large-scale circulation impacts on turbulence in the identical way to the LES experiments, including the one-way interaction between the shear associated with the EUC and the turbulent production.

3.1 Comparison of OM4-1d and LES

We start by confirming that the OM4-1d and LES models produce a similar temperature and current structure (Figure 7). The figure shows the evolution of temperature and zonal current during the 35 day simulation, which runs from October 2, 1985 to November 6, 1985. The OM4 model does a reasonable job simulating the temperature and current evolution at both the equatorial site and the 3° N site compared to the LES. To more directly examine the impact of the parameterized mixing in OM4-1d versus the LES, we next examine the time series of turbulent vertical temperature (heat) flux and its induced temperature tendency over a seven day time slice from the full experiment (October 28 through November 5). While the main patterns between the LES and OM4-1d are similar, which is not surprising given the agreement in the mean temperature, there is a very clear difference in the diurnal variation and vertical structure of the vertical temperature fluxes (Figure 8). Of particular note is the more rapid penetration of the temperature flux each night, which yields more rounded structures in the vertical temperature fluxes

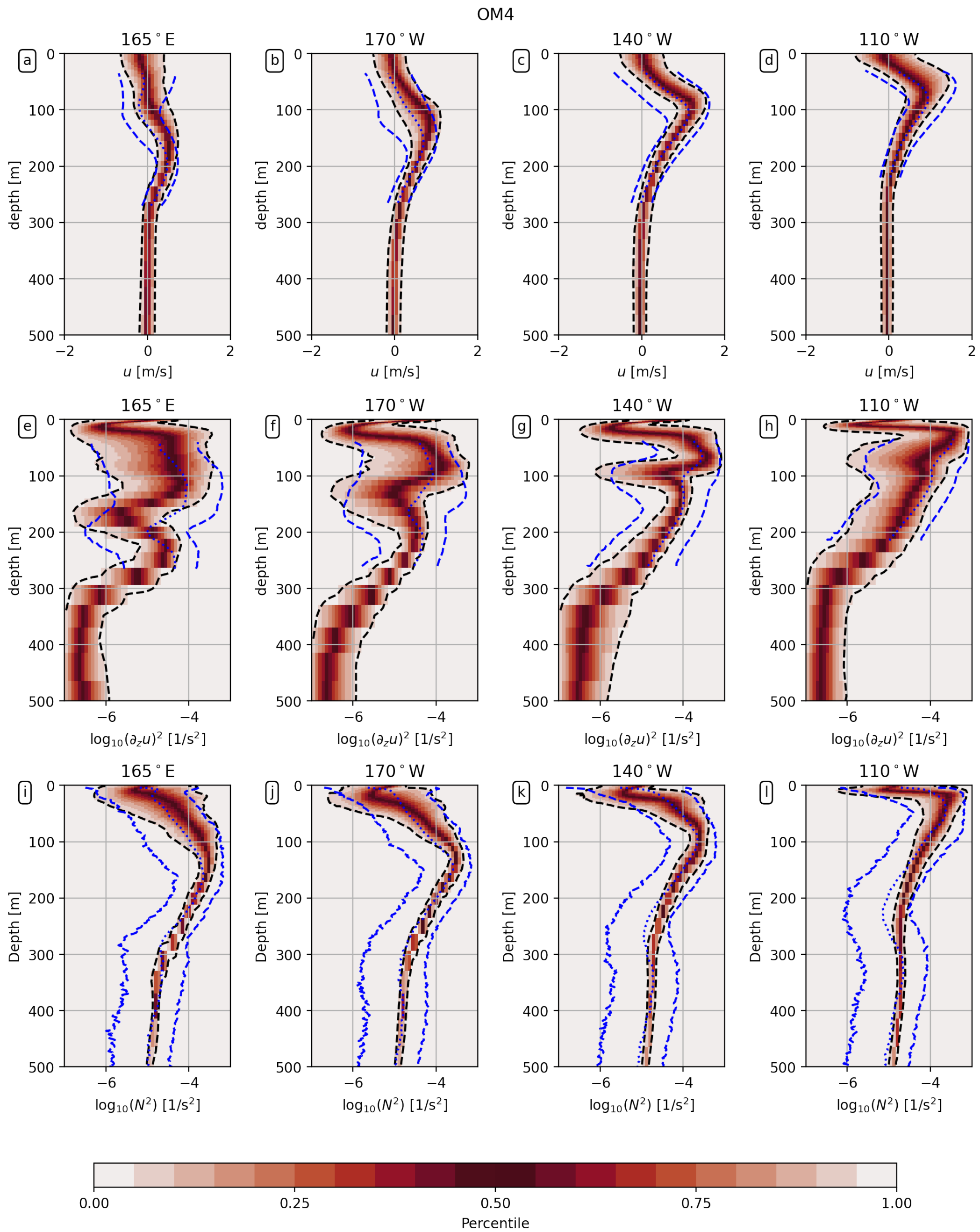

Figure 6. As in Figure 5, but for the OM4 model. The black dashed trace represents the 5th and 95th percentile, while the blue dashed tracers represent the similar values from the observations. The blue dotted trace represents the median of the observations (see Figure 5).

in OM4-1d. In the LES the temperature flux depth penetration each night occurs more gradually, resulting in sharper, pointed features and induced tendencies than in OM4-1d.

To better understand these differences we diurnally composite both the vertical temperature flux field and the induced temperature tendency (Figure 9). The composites show a repeated daily cycle of temperature tendency and temperature flux centered (hour 0) at the local peak of

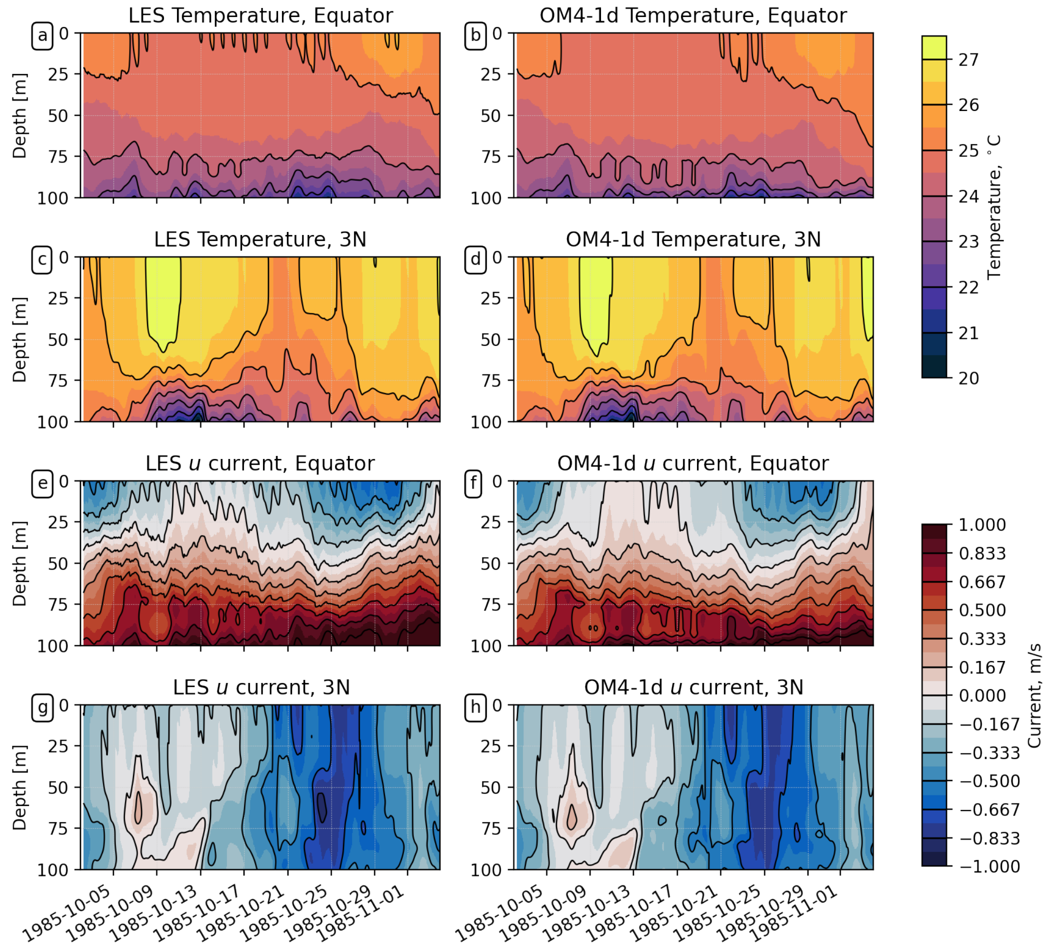

Figure 7. LES (left column) and OM4-1d (right column) comparison for temperature (upper set of four panels) and zonal current speed (lower set of four panels) at 140°W. Results shown for the equator (first and third row) and 3°N (second and fourth row). LES provided from Whitt et al. (2022).

solar heating. The downward temperature flux in the LES (panels a-d) clearly preserves the regular peaked structure, while the rounded nature of the OM4-1d (panels e-h) is seen in both the raw time series data and the diurnal composite. A clear bias in the OM4-1d temperature flux is that it predicts much too strong downward temperature fluxes at hour 0, when the LES shows a near complete shut down of vertical mixing (reflected by much stronger positive temperature tendency between 10 and 50 meters in OM4-1d). It is obvious from these runs that a major bias emerges in the diurnal pattern of OM4 vertical mixing and temperature tendency. We also show the time averaged fluxes over simulation period (Figure 10), which shows that the net downward temperature flux peaks about 10% larger in OM4-1d (red dashed line) compared to the LES (black line).

3.2 Modifying OM4-1d and evaluating remaining difference from LES

The ePBL mixing energy is parameterized from $m_* u_*^3$, where m_* is the proportionality between the vertically integrated rate of conversion between TKE and potential energy due to turbulent mixing in gravitationally stable stratication and u_* is the wind friction velocity. The m_* parameterization used by OM4-1d significantly overestimates the net vertical temperature flux during the daytime in the upper 30 m (as demonstrated at hour 0 in Figure 9). We now explain

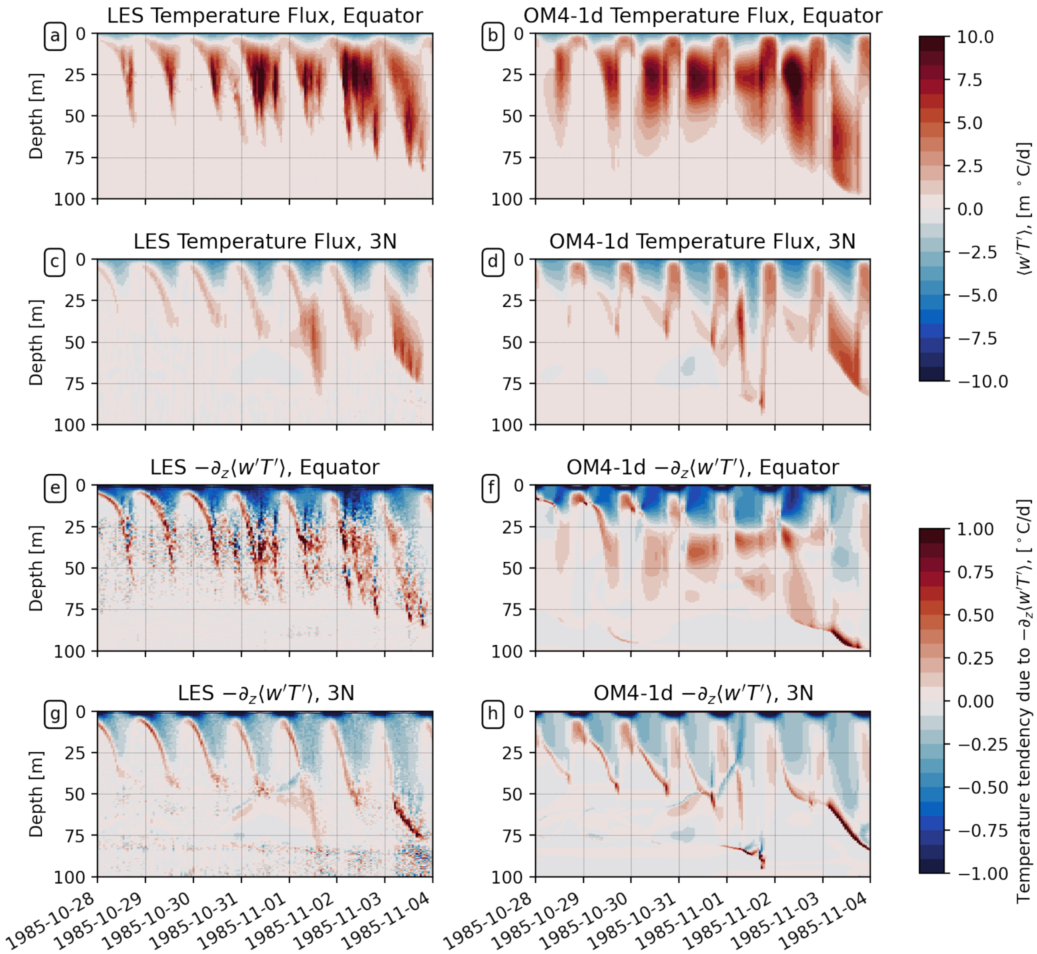

Figure 8. One-week subset of LES (left column) and OM4-1d (right column) comparison for vertical turbulent temperature flux (upper set of four panels) and its induced temperature tendency due to convergence (lower set of four panels) at 140°W. Results shown for the equator (first and third row) and 3°N (second and fourth row). LES provided from Whitt et al. (2022).

the reason for this disagreement between the ePBL temperature flux and the LES, and a strategy to improve the diurnal cycle of the vertical mixing in OM4. The ePBL mixing scheme constrains the depth of the ocean surface boundary layer based on the energetics associated with turbulent mixing of a stratified fluid (Reichl & Hallberg, 2018). In Reichl and Hallberg (2018), the formulation of the parameterization for mixing energy is developed using numerical experiments that experience constant surface forcing (wind stress and surface bouyancy fluxes). The resulting parameterization therefore satisfies a condition where the boundary layer depth, buoyancy flux, and mechanical forcing terms all vary relatively slowly in time. The mean properties (e.g., shear and stratification) are not explicitly considered by ePBL, and instead the turbulent fields are parameterized only using information about the surface forcing and the boundary layer depth.

The overestimation of the temperature flux in the daytime by ePBL happens when there is a rapid change in the forcing conditions, mean shear and stratification, and the boundary layer depth over the diurnal cycle. This rapid change means that these quantities are constantly out of equilibrium and that the properties of the turbulence can no longer be reliably parameterized only considering the surface forcing. For example, as the sun rises the boundary layer can remain deep

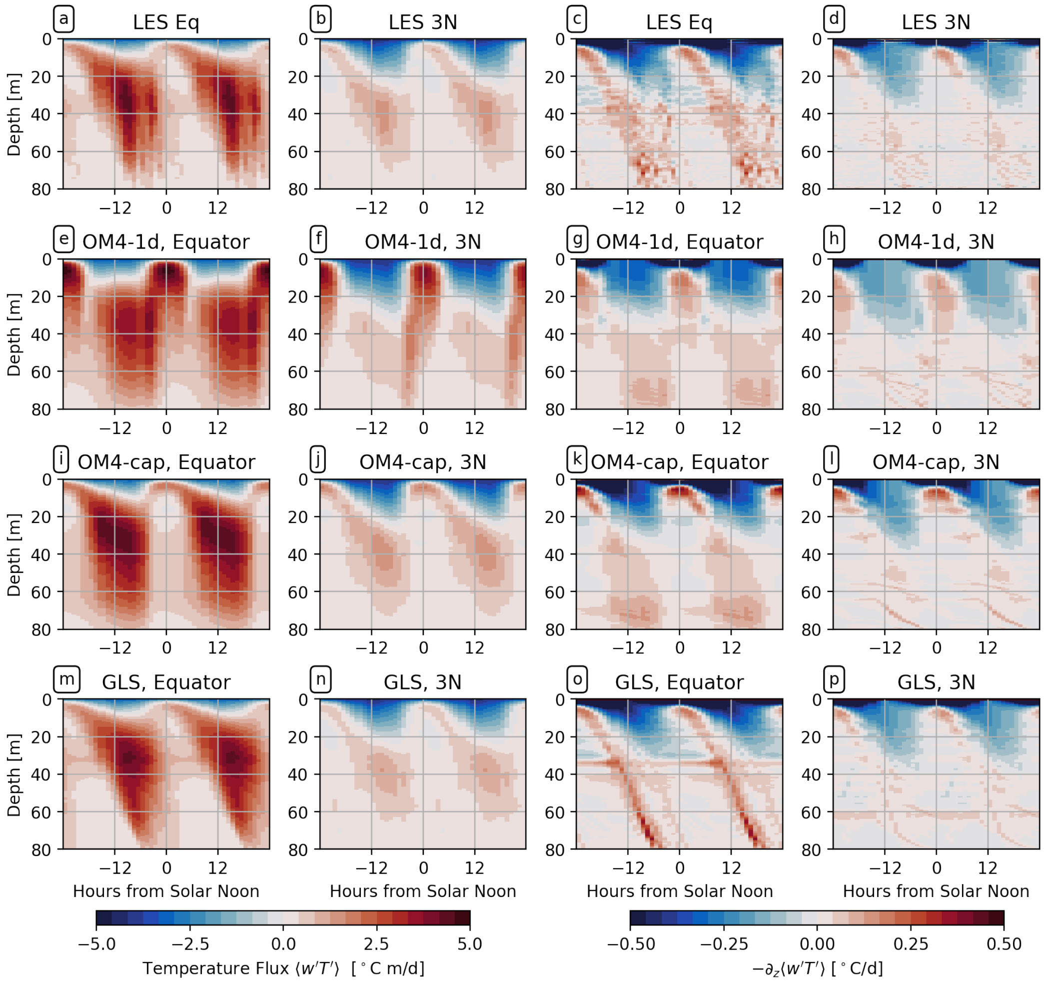

Figure 9. Diurnal composite of LES (1st row), OM4-1d (2nd row), OM4-cap (3rd row), and GLS (4th row) comparison for vertical turbulent temperature flux (positive downward, first and second column) and temperature tendency due to turbulent temperature flux convergence (third and fourth column) at 140°W. Results shown for the equator (first and third column) and 3°N (second and fourth columns). LES provided from Whitt et al. (2022).

for a couple of hours due to the pre-existing fossil turbulence. The Reichl and Hallberg (2018) mixing energy parameterization overestimates the mixing energy because the energy scales with the boundary layer depth, but the boundary layer depth is large and has not yet retreated to reflect the strong surface heating conditions. Hence, the m_* predicted by ePBL is only accurate after the buoyancy gradient has a chance to establish and the boundary layer depth has adjusted to the surface forcing conditions together with the turbulent boundary layer.

A suitable prescription for m_* is difficult in the presence of these rapidly changing conditions. The difficulty arises since the assumptions that underpin ePBL's ability to predict boundary layer depths break down within this region of marginal stability and rapidly changing conditions. However, separate column model tests reveal that by setting m_* in ePBL at the equator to 0, and only using the JHL shear driven mixing scheme, the OM4-1d model can predict fluxes and temperature that are much more similar to the LES. The reason for this agreement is because the JHL scheme is developed for predicting diffusivities for shear-driven mixing processes, which

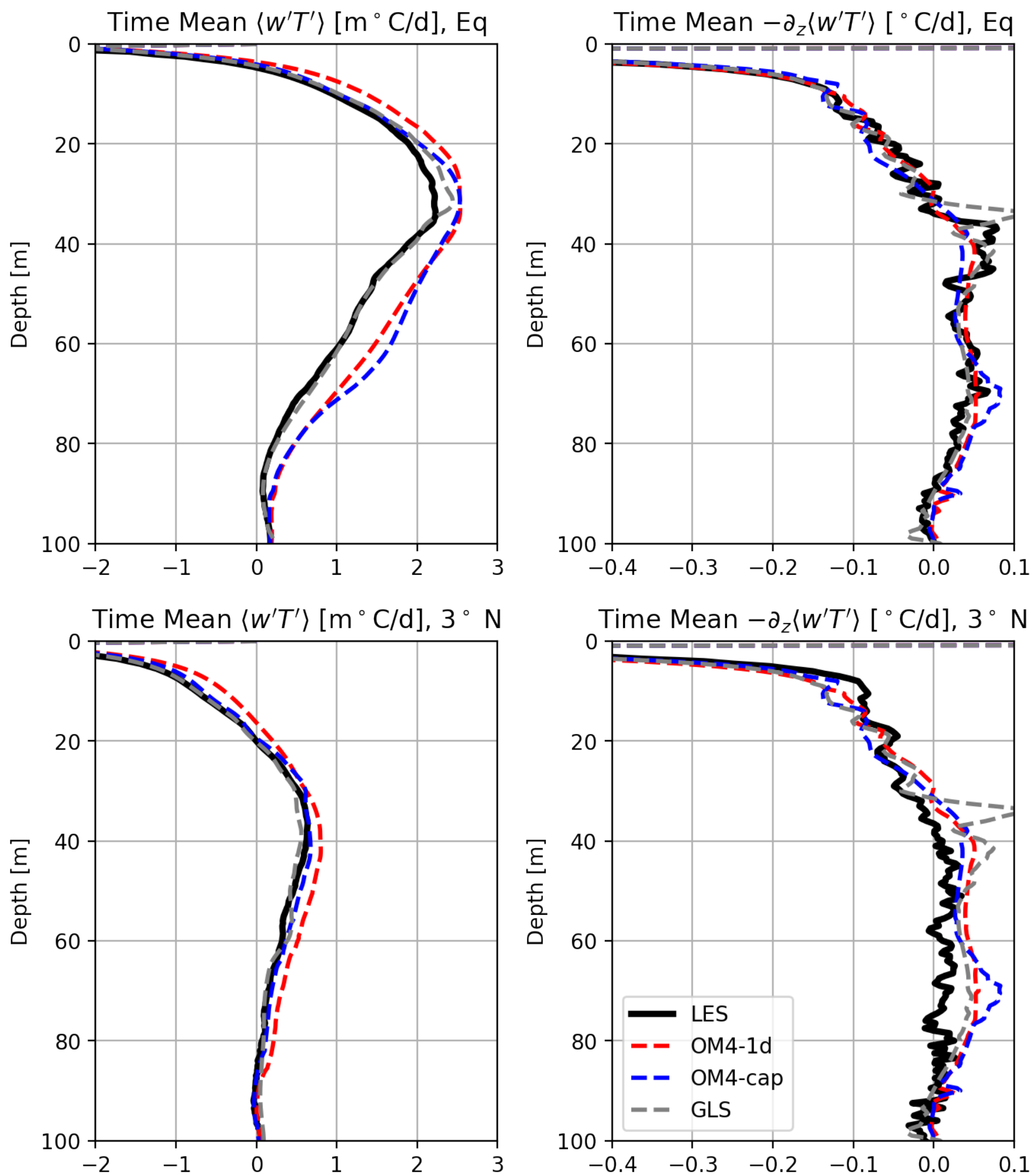

Figure 10. Time mean of LES (black), OM4-1d (red dashed), OM4-cap (blue dashed), and GLS (gray dashed) comparison for vertical turbulent temperature flux (positive downward, first column) and temperature tendency due to turbulent temperature flux convergence (second column) at 140°W. Results shown for the equator (top row) and 3°N (bottom row). LES provided from Whitt et al. (2022).

dominate the turbulence within this region. Many other tests of the ePBL m_* prescription in the column model reveal a practical fix for the overmixing. Namely, we cap the ePBL value of m_* at a value close to 1 but much less than 10. Since the value of m_* outside ± 5° is almost always less than 1.25, the cap of 1.25 is chosen. We perform additional sensitivity studies to the precise value of the cap that suggest 1.25 is a reasonable choice . In particular, prescribing that $m_* \leq 1.25$ does not degrade the performance of ePBL outside of this equatorial region. Future work will focus on more optimal approaches to modeling m_* and its interaction with JHL in the tropics (and elsewhere), but at present the cap of $m_* = 1.25$ appears to be a practical and reasonable approach and is thus adopted here.

Figure 9 (3rd row) demonstrates that this m_* cap provides a significant improvement to the OM4 temperature flux bias. We see that these runs are much closer to the LES (top row) for predicting the temperature flux and its induced temperature tendency than the original OM4. The $m_* \leq 1.25$ cap achieves the goal of shutting off the overly strong ePBL mixing during the daytime and allows the JHL scheme to dictate the mixing coefficients. We also see that the time mean vertical temperature flux is improved relative to OM4-1d (Figure 10), especially in the upper 20 m at the equator and throughout the column at 3° N. While the OM4-cap scheme is an improvement over OM4, the temperature flux still deepens too rapidly at night (about 6 hours after solar noon) compared to the LES at the equator (see first column).

To explain this rapid deepening of the temperature flux (and tendencies) in the OM4 and OM4-cap experiments requires revisiting the theory that underpins the JHL shear mixing scheme. One assumption in developing the set of equations employed by JHL is that the turbulence develops rapidly compared to the mean flow (e.g. the TKE tendency term is ignored and a steady-state equation for TKE is solved). This simplification of the dynamics helps the JHL model to be less sensitive to model details like timesteps and vertical resolution, but turns out to be the cause of the too-rapid penetration of the night time temperature flux. This feature is demonstrated by comparing the OM4-cap results to a separate one-dimensional model test that uses a full second moment closure (SMC, following Umlauf & Burchard, 2003) with a TKE time tendency via the General Ocean Turbulence Model (GOTM, `gotm.net`). In the SMC simulation, the slower penetration of the vertical temperature flux observed in the LES is recovered by the column model (Figure 9, bottom row). We verify the important difference between SMC and JHL is the turbulence storage term by iterating the TKE and length equations in the SMC model 10 times within each model time step, effectively bringing the turbulence in SMC to equilibrium as is prescribed in JHL. The too-rapid penetration of the vertical temperature flux in JHL is recovered by SMC with the steady-state turbulence, indicating that the adjustment time for the turbulence to the mean state is important for getting these high-frequency characteristics of turbulent fluxes. This exercise indicates a role of the TKE adjustment time (storage term) on the vertical temperature flux in deep-cycle turbulence. Further investigation into the simulation in OM4 of the diurnal cycle of turbulence with SMC or an additional TKE storage term in JHL will be undertaken in future research, as it requires new research efforts to fully implement either approach in OM4.

4 Evaluating and adjusting upper ocean parameterizations in OM4: an OGCM approach

The evaluation of OM4-1d against LES and establishment of the OM4-cap ePBL update yield confidence in an implementation of improved vertical mixing in OM4 from a process perspective. We now present an evaluation of OM4 with the ePBL m_* cap of 1.25 to evaluate how the improved representation of vertical mixing impacts the 3d simulation. To do so, we rerun OM4 with the only change being the m_* cap for both the full JRA55-do v1.5 cycle experiment (with the identical configuration to OM4) and for the experiment from 1999-2008 with the z_* configuration and the high-frequency virtual mooring output.

4.1 Evaluating ePBL-cap in OM4, OGCM approach

We first analyze the impact of the ePBL $m_* \leq 1.25$ cap in the percentile heatmap figures from the OM4 simulations with the virtual buoys (Figure 11), now including the dashed line contours from OM4 (in cyan) to compare for reference. We see very little impact in the distribution of the mean currents between the OM4 and OM4-cap run, however, the shear and stratification plots do show some improvements in the upper 50m. This result indicates that the OM4-cap model does have different variability in terms of less tendency to form very weak stratification and shear at these shallow depths (a direct consequence of capping m_*). However, we see relatively small differences between OM4 and OM4-cap in other aspects of the simulation, with the cyan and black curves following each other quite closely. We next evaluate the difference between OM4, OM4-cap, and the climatological observations (Figure 12). The result is unexpected, in which the OM4-cap result ends up being slightly less skillful than OM4 in terms of both simulating temperature and salinity stratification (compare to Figure 2). This result suggests that there must be other issues unrelated to the processes simulated in the LES, since the OM4-cap model was an improvement over OM4 in comparison with the LES. It also suggests there may be some compensating biases in the OM4 model, as the improved mixing relative to the LES results in a slightly degraded solution in the full 3d simulation.

4.2 Additional OM4 modifications

In the previous sections we described the disadvantages of using observations to directly tune parameterizations in a full OGCM. However, we wish to evaluate sensitivity of the model biases to other parameterization choices now that the LES has rendered confidence in the OM4-cap upper ocean vertical mixing schemes. In total we simulated several dozen additional configurations of OM4 and analyzed how the results compared to the biases presented for OM4 and OM4-cap. At the conclusion of this parameterization sweep, we identify two additional choices for the ocean mixing parameterizations that have particular influence on the tropical ocean biases.

The first change to the model is the addition of a new choice for computing the JHL mixing coefficients (parameter setting “VERTEX_SHEAR = True” in MOM6), where the model temperature, salinity, and currents are interpolated to the horizontal C-grid cell vertices instead of the default of interpolating the currents to the C-grid cell centers. A large motivation for this change is to avoid checkerboard patterns in the mean fields related to numerical noise issues that traditionally plague Richardson number based mixing schemes. The second change we identify is to disable the large background viscosity of 10^{-4} m^2 s^{-1}. The high viscosity setting exists in OM4 despite having no physical justification, perhaps related to historical reasons for numerical stability that are no longer necessary in MOM6. We also found sensitivity of the stratification bias to settings in OM4 for the vertical coordinate and the MLE restratification parameterization, but these impacts were smaller and thus are saved for further analysis in future work.

We examine the impact of these two modifications separately (not shown). While the vertex shear choice is advantageous for its goal of mitigating grid scale noise, it does not have significant impact on the time mean stratification. However, removal of the enhanced background viscosity has a large impact on the zonal shear, especially in the eastern mooring location (110° W). The reduction of the background viscosity leads to a less diffuse EUC with increased zonal shear, which leads to reduction in the Richardson number and increased diffusivity from the JHL parameterization. Reducing the background viscosity therefore results in an overall improvement to the large scale mean stratification compared to the original OM4 model. Therefore, we next present results that analyze the three updates to OM4 together, which includes the $m_* \leq 1.25$ cap, the updated JHL shear mixing scheme, and the reduced background viscosity. This version of OM4 is denoted OM4up for the remainder of this manuscript.

The OM4up configuration yields improvements over OM4 in many aspects of the simulation based on the metrics analyzed here. In particular, we see improvements in the distribution of shear and stratification (primarily driven by reducing the background viscosity, see Figure 13), which leads to a much better representation of the zonal (and particularly eastern basin) stratification bias between 50 and 200 m depth. The peak strength of the EUC in its eastern extent is also better captured, the primary reason for this improvement being that the enhanced background viscosity in OM4 was contributing to an excessively diffuse EUC. Better capturing the EUC and its shear in OM4up allows improved mixing to be predicted by JHL, since this improved shear is provided as an input to the parameterization. We see a significant overall improvement in OM4up compared to OM4 in the mean temperature stratification bias (Figure 14). This result suggests that similar reasons for the biases targeted in the Pacific Ocean were affecting the other tropical basins. The global r^2 improves from 0.855 in OM4-cap to 0.923 in OM4up (compared to 0.878

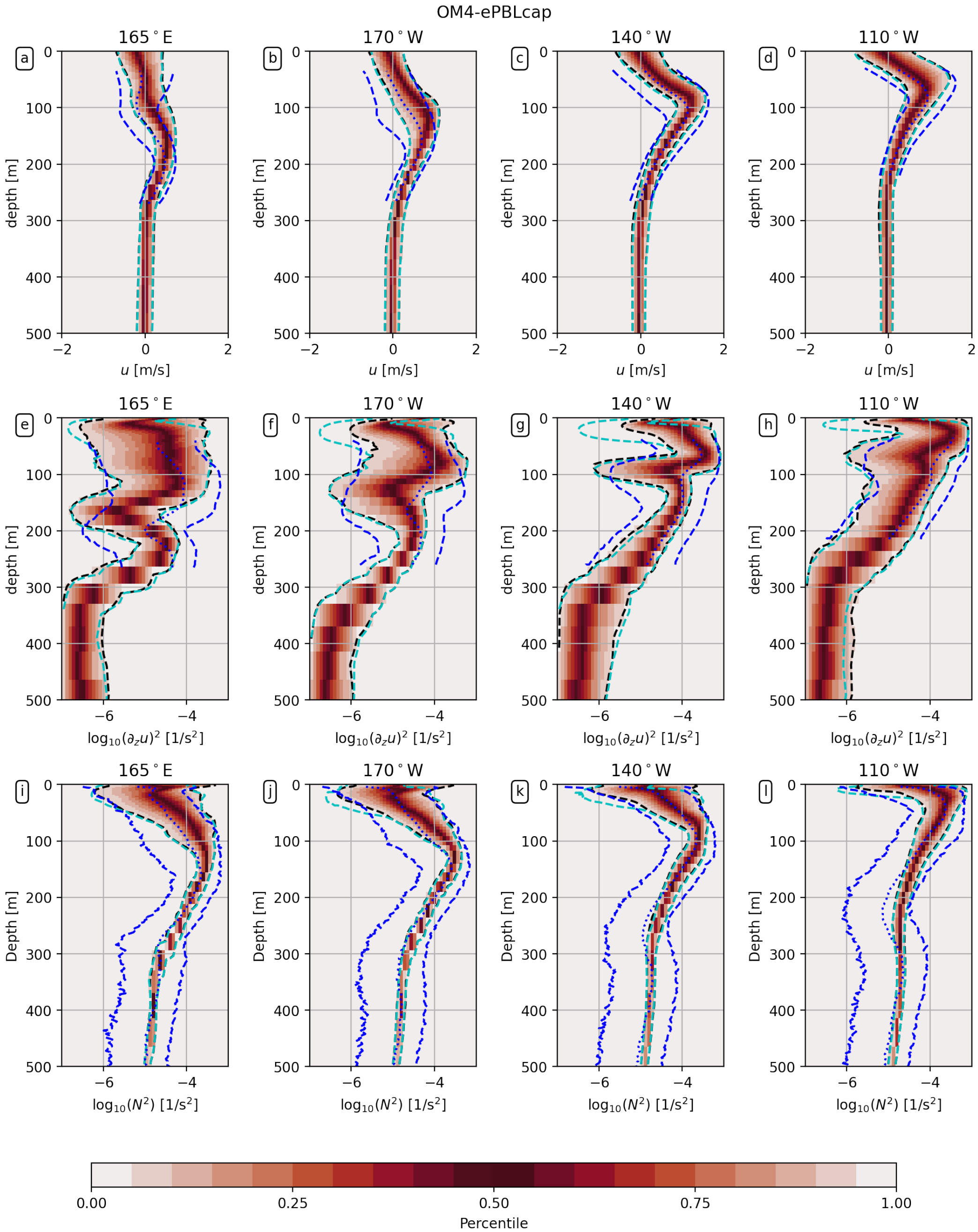

Figure 11. As in Figure 6, but for the OM4 model updated with the $m_* \leq 1.25$ cap in ePBL. The black dashed trace represents the 5th and 95th percentile, while the blue dashed tracers represent the similar values from the observations. The blue dotted trace represents the median of the observations (see Figure 5). The cyan dashed line represents the 5th and 95th percentiles in the original OM4 results (see Figure 6).

in OM4) and RMSE improves from 0.0184 to 0.0131°C/m (compared to 0.0168°C/m in OM4). We see similar improvements in salinity stratification, with r^2 improving from 0.846 to 0.884 (compared to 0.879 in OM4) and RMSE improving from 0.0050 to 0.0033 ppt/m (compared to 0.0045 ppt/m in OM4). Finally, we note that the improvements in temperature and salinity stratification are reflected in the mean fields as well, with RMS difference in temperature improving from 0.7289°C

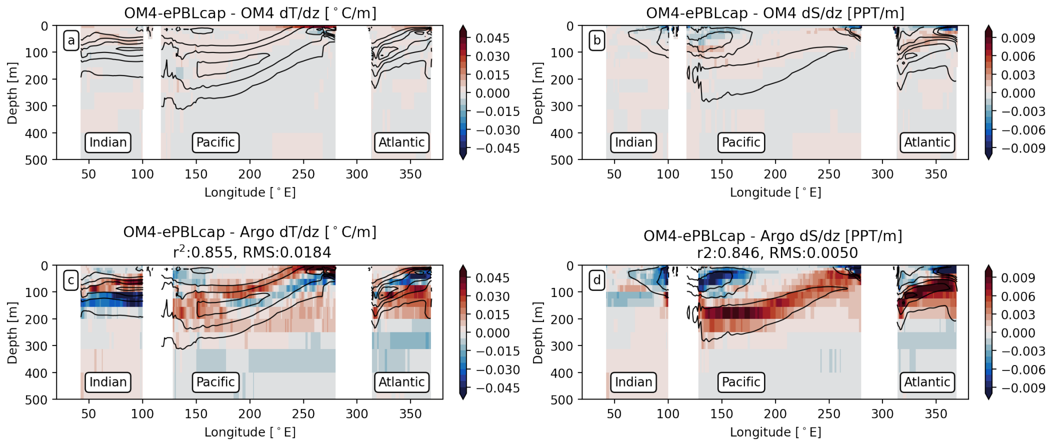

Figure 12. As in Figure 4, but for the OM4 model updated with the m_* cap in ePBL.

in OM4 to 0.6752°C in OM4-up and salinity improving from 0.2637 ppt in OM4 to 0.2325 ppt in OM4-up (Figure 15).

These results suggest that despite the LES results providing an improved diurnal cycle in OM4-cap, it was the impact of the large background viscosity that contributed to the eastern Pacific stratification bias. Ultimately this high background mixing was degrading the currents and shears that feed into driving the JHL mixing parameterization. We note that shallow biases in the EUC core remain in OM4up in the western basin, perhaps even being degraded relative to OM4 at 165° E and 170° W. This shoaling of the EUC in the west suggests that the elevated viscosity may potentially help deepen the western EUC toward observed values in OM4. We do not pursue enhancing the viscosity in the west in this work, as a skillful parameterization of potentially enhanced viscosity first requires research to understand the physical processes. We also evaluated the OM4up changes for any potential major impacts outside of the equatorial region, which did not reveal any obvious problems.

4.3 Remaining sources of bias and the role of vertical resolution

While the choices implemented in OM4up lead to an improved tropical ocean climate relative to OM4, significant work remains to completely address the tropical mixing, thermocline, and stratification biases. We propose that the LES exercise has imparted confidence in the OM4up configuration in terms of its vertical mixing scheme, but despite these improvements several biases remain in OM4up compared to the observations. We now ask the question, what potential issues may drive the remaining biases?

One candidate is the remaining phase difference in vertical heat fluxes between OM4-cap and the GLS 1d mixing (Figure 9). However, the small impact of OM4-cap relative to OM4 suggests these improvements would also have small impacts on climatological features in these OGCM simulations. Another potential candidate is the hybrid ($z_* - \sigma_2$) vertical coordinate in OM4. The σ_2 component of the coordinate leads to thicker layers (coarser vertical spacing in meters) in the western Pacific than in the eastern Pacific since the near surface waters are less stratified (note the upper 200 meters in the western and eastern Pacific Ocean in Figures 1 and 2). However, we conclude that this is not the primary source of remaining bias since the OM4up model is tested here both with the hybrid and $z*$ coordinate. Another possible source of bias is the MLE restratification parameterization. The tropical bias in OM4 was very sensitive to choices in MLE (not shown). However, this sensitivity is significantly reduced in OM4up, suggesting there may have been some feedback between the original OM4 model and its MLE. The source of the remain-

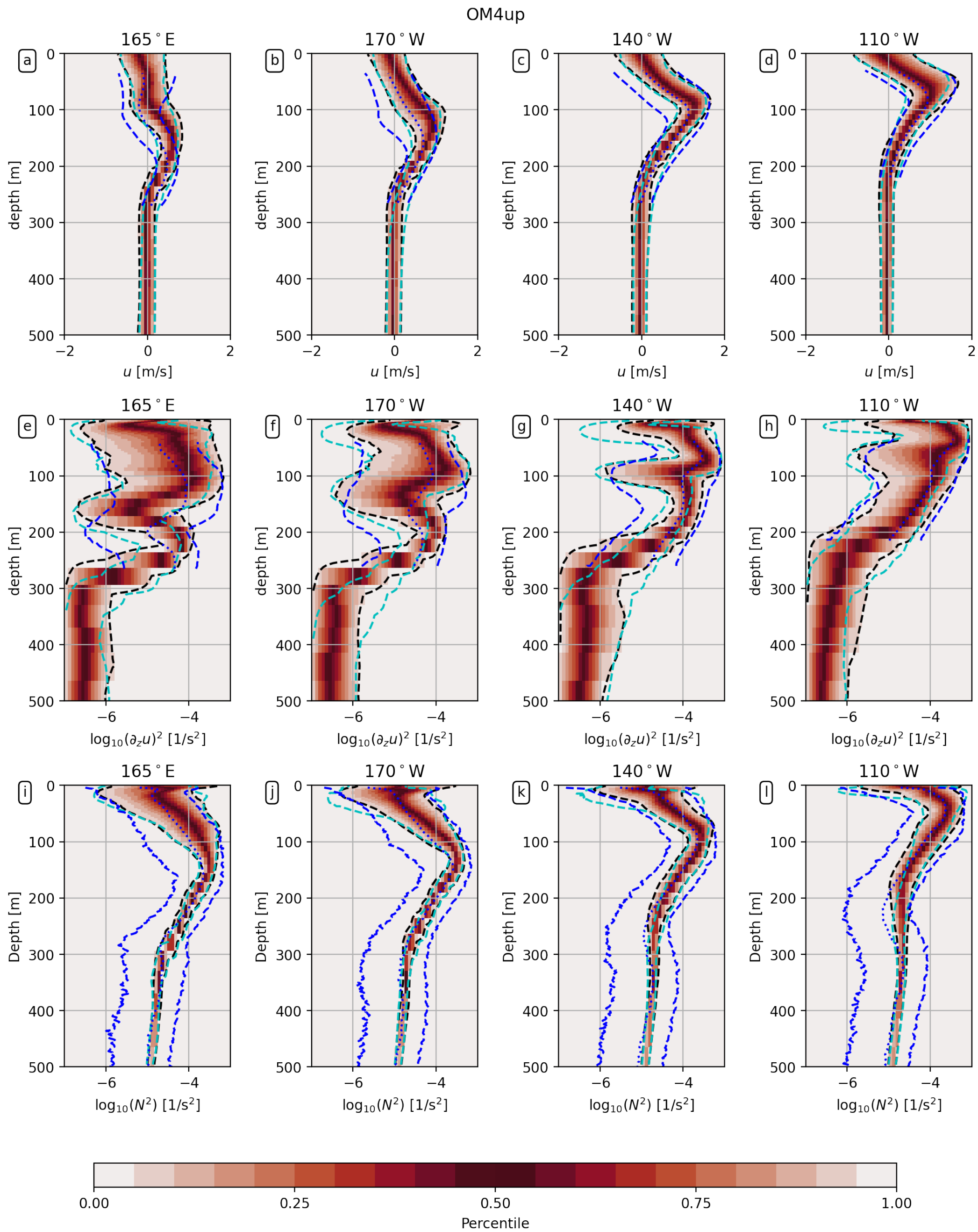

Figure 13. As in Figure 6, but for the OM4 model with all updates described in this paper. The black dashed trace represents the 5th and 95th percentile, while the blue dashed tracers represent the similar values from the observations. The blue dotted trace represents the median of the observations (see Figure 5).

ing shallow thermocline and EUC biases therefore remains unclear from this study, though forcing errors and additional mixing process biases are likely potential culprits.

We performed one additional experiment in an effort to improve the simulation through enhancing the number of vertical grid levels by a factor of three. In OM4 the vertical z_* grid spacing is set with a resolution function that increases gradually from 2 m at the surface to signifi-

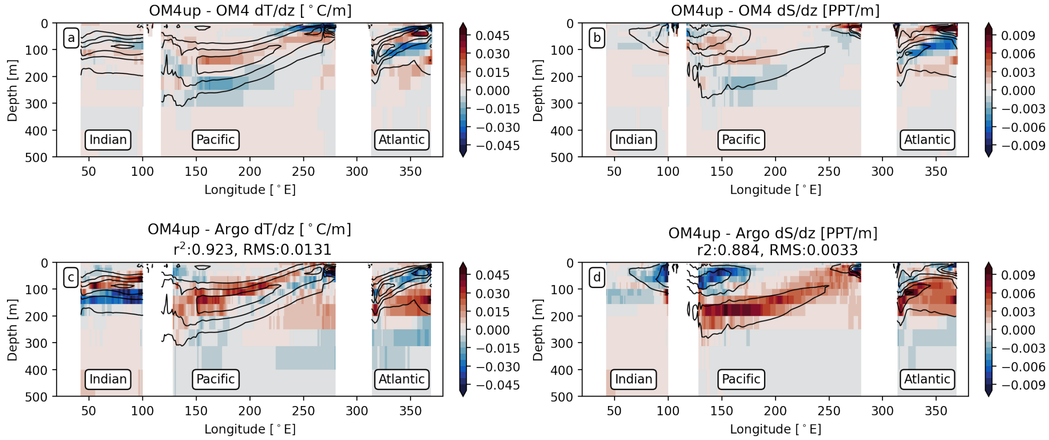

Figure 14. As in Figure 4, but for the OM4 model with all updates described in this paper.

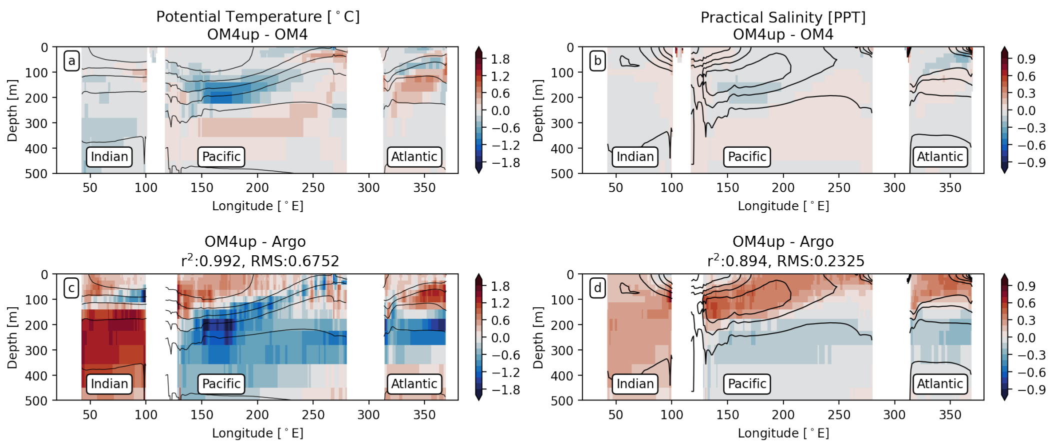

Figure 15. As in Figure 3, but for the OM4 model with all updates described in this paper.

cantly thicker levels at depth. The OM4up-225 model is run with 225 vertical layers (increased from the original 75), where the OM4up-225 grid thicknesses start from the same 2 m spacing near the surface as OM4 (and OM4up). The vertical grid spacing in OM4up-225 increases at depth much slower than OM4, and it maintains relatively fine grid spacing throughout the upper 500 m. Since this simulation is computationally more expensive (in terms of runtime and data storage), we only analyze it in the 10 year experiments (1999-2008) and present results for the variability heat maps (Figure 16). The increase in resolution is understood by comparing the y resolution at depth in Figure 13 with Figure 16. The interior (e.g., 500 m to 100 m) shear and stratification heat maps reveal significant differences between OM4up and OM4up-225. In particular, OM4up-225 has increased high shear events throughout this entire region (observations in blue are much closer to OM4up-225 in black than OM4up in cyan in the middle row). OM4up-225 also has increased variability in stratification at depth (comparing black and cyan in the bottom row), though still much less than the observations (comparing black and blue in the bottom row). The stratification below the pycnocline in the western equatorial Pacific is reduced to a level closer to observations in OM4up-225, which is an intriguing result due to the importance of these watermasses in the formation of tropical oxygen minimum zones (see Stramma et al., 2010). We see the additional layers do not significantly impact the near surface simulation, which is not surprising since the same resolution is used in the upper 20 m and the impacts are only seen below this depth.

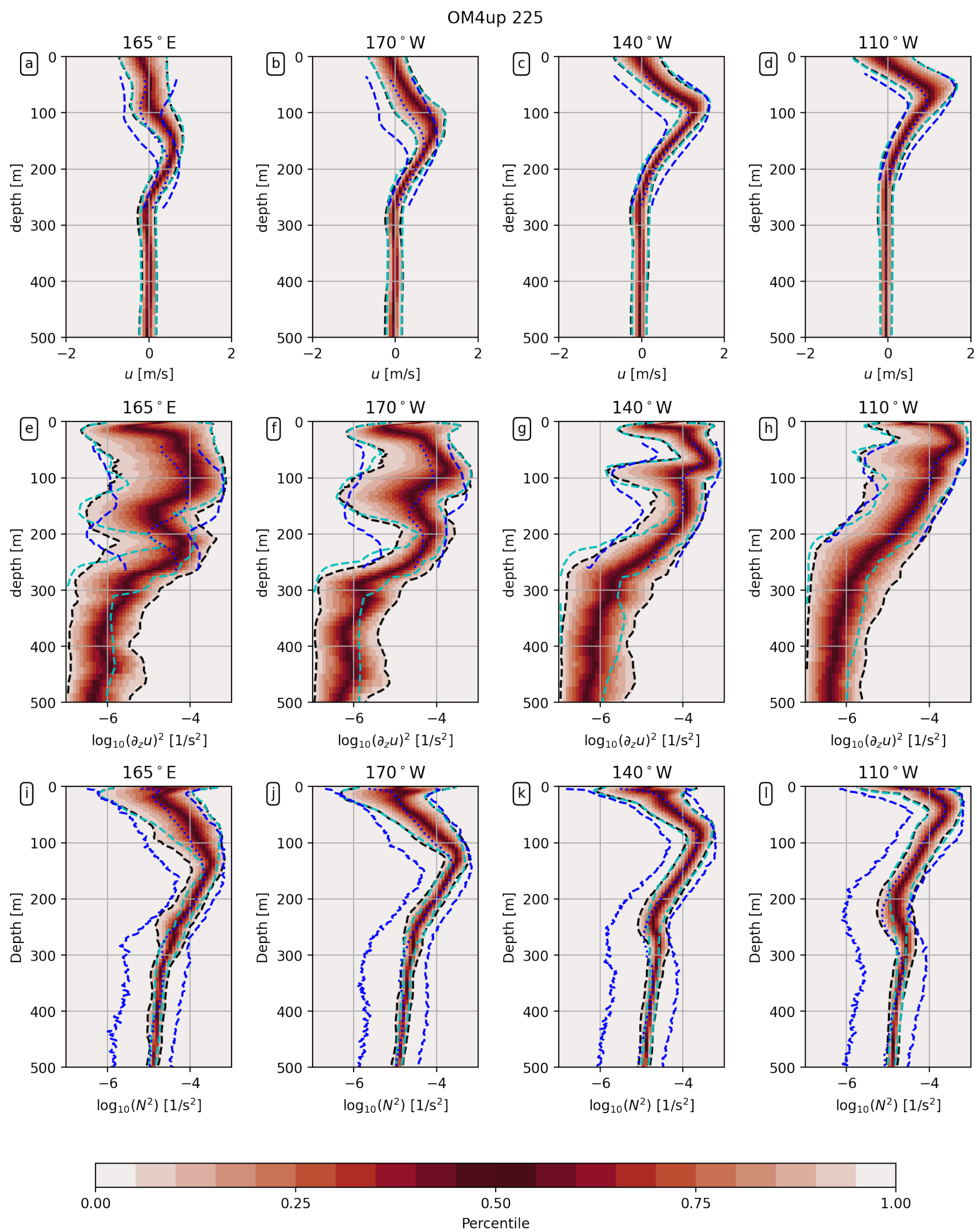

Figure 16. As in Figure 6, but for the OM4 model with all updates described in this paper and 225 vertical levels. The black dashed trace represents the 5th and 95th percentile, while the blue dashed tracers represent the similar values from the observations. The blue dotted trace represents the median of the observations (see Figure 5). The cyan dashed line represents the 5th and 95th percentiles in the original OM4up results (see Figure 13).

We now explore aspects of the OM4up-225 experiment relative to OM4 and OM4up to better understand how refined vertical grid spacing can affect the interior solution. The first thing we show is the heatmap of the occurrences of Richardson numbers (Figure 17). Since Ri was not saved during the model runs, it is instead approximated diagnostically from two hourly mean N^2 and S^2 (we also directly explore the model's shear-driven diffusivity to confirm that this approach is a reasonable approximation for the two-hourly mean Richardson number). The Ri values are binned into 50 evenly spaced increments between $0 < Ri < 1$ for each of the three models and in the following analysis we compare the count of occurrences within each bin. When we compare the OM4 and OM4up models (upper and middle row), we can see very clearly that OM4up indeed has significantly increased occurrence of lower (less stable) Richardson number fed into the JHL mixing parameterization compared to OM4. In fact, throughout the lower flank of the EUC we see many lower Richardson number events (e.g., at 165° E and 170° W). However, when we increase the resolution by tripling the number of vertical layers, we see that significantly more mixing events (Richardson number 0.25 or lower) occur in the model (bottom row). This result suggests that the Richardson number based parameterizations could depend on the resolution to improve performance in models with coarser vertical spacing. We also show the distribution of net diffusivity values in the three models (Figure 18). The diffusivity profiles clearly show that OM4up-225 has significantly more mixing events below about 100 m compared to OM4 and OM4up, when the JHL parameterization is provided with lower Richardson number values.

We conclude by looking at the vertical structure and temporal dependence of these low Richardson number mixing events from a two year subset of the model's diffusivity from the three simulations (Figure 19). We see that these low Richardson number/high diffusivity events (mapped in red) can be large-scale (e.g., vertical extents that span several model layers), and can persist for several months. This result suggests that the impacts of these low occurrence mixing events can be long lasting in the model, and can potentially contribute to shaping characteristics of the lower flank of the thermocline and the EUC on long term timescales. While we do not pursue enhancements to the JHL scheme to account for vertical resolution here, it is clearly worth exploring in future work to improve the comparison with data and the formation of the lower thermocline waters in the tropics.

5 Conclusions and Outlooks

In this study we utilized a variety of methods to analyze causes for equatorial stratification and circulation biases (see Figures 1 and 2) in the NOAA Geophysical Fluid Dynamics Laboratory OM4 ocean model (Adcroft et al., 2019). We first compared the OM4 mixing parameterizations in a column model configuration of OM4 directly to LES (Whitt et al., 2022). This comparison led us to correct a significant bias in the diurnal cycle of mixing in OM4 (Section 3, Figures 9). However, when implementing the correction in the full three-dimensional ocean circulation model (OGCM), we found little impact on the time-mean biases. We did not investigate the impact of the improved diurnal cycle of mixing in a coupled ocean-atmosphere model (CGCM), where the atmospheric boundary layer has a chance to respond to the improvements in the oceanic boundary layer.

We found that the primary reason for OM4's stratification bias in the eastern equatorial Pacific is related to a high background viscosity. The large viscosity results in poor simulation of the vertical shear that is provided as an input to the shear-based mixing parmeterization. By eliminating the high background viscosity, we substantially improve the simulated stratification in this region (Figure 14). We also found that increasing the number of vertical layers in OM4 has the potential to significantly impact the mixing and improve interior stratification, though whether or not this mixing results in improved currents compared to OM4 could not be confirmed from the present set of ocean observations since ADCPs are limited to 50-250m depth and most differences are seen between 500 m and 250 m.

While evaluation of these mixing parameterizations and its impact on equatorial stratification biases has been specific to OM4, the implications of these results are much broader. First,

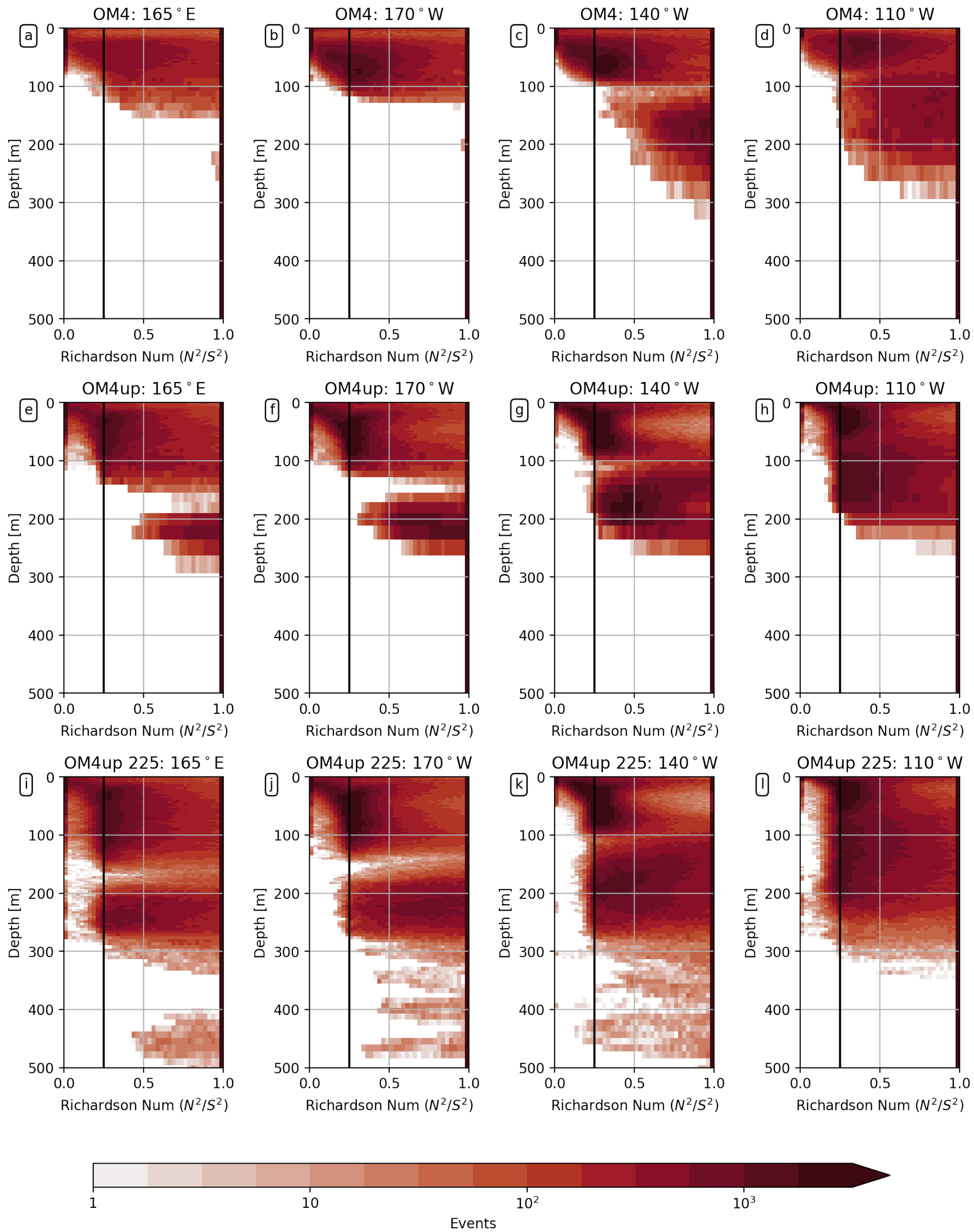

Figure 17. Discrete occurrence event heatmap for Richardson number in the OM4 model, the updated OM4 model, and the updated OM4 model with higher vertical resolution (225 levels).

we have demonstrated the importance of accurately simulating the EUC for capturing the mixing and tropical stratification, further elucidating importance of the fully interactive and three-dimensional characteristics of this region for its simulation. Second, we have emphasized the utility of the high-fidelity tropical LES (such as Whitt et al., 2022) for evaluating one-dimensional mixing parameterizations despite the highly three-dimensional nature of this region (see also Large & Gent, 1999). We find that the one-dimensional model evaluations of ocean mixing parameterizations are an important complement to OGCM experiments and help guide parameteriza-

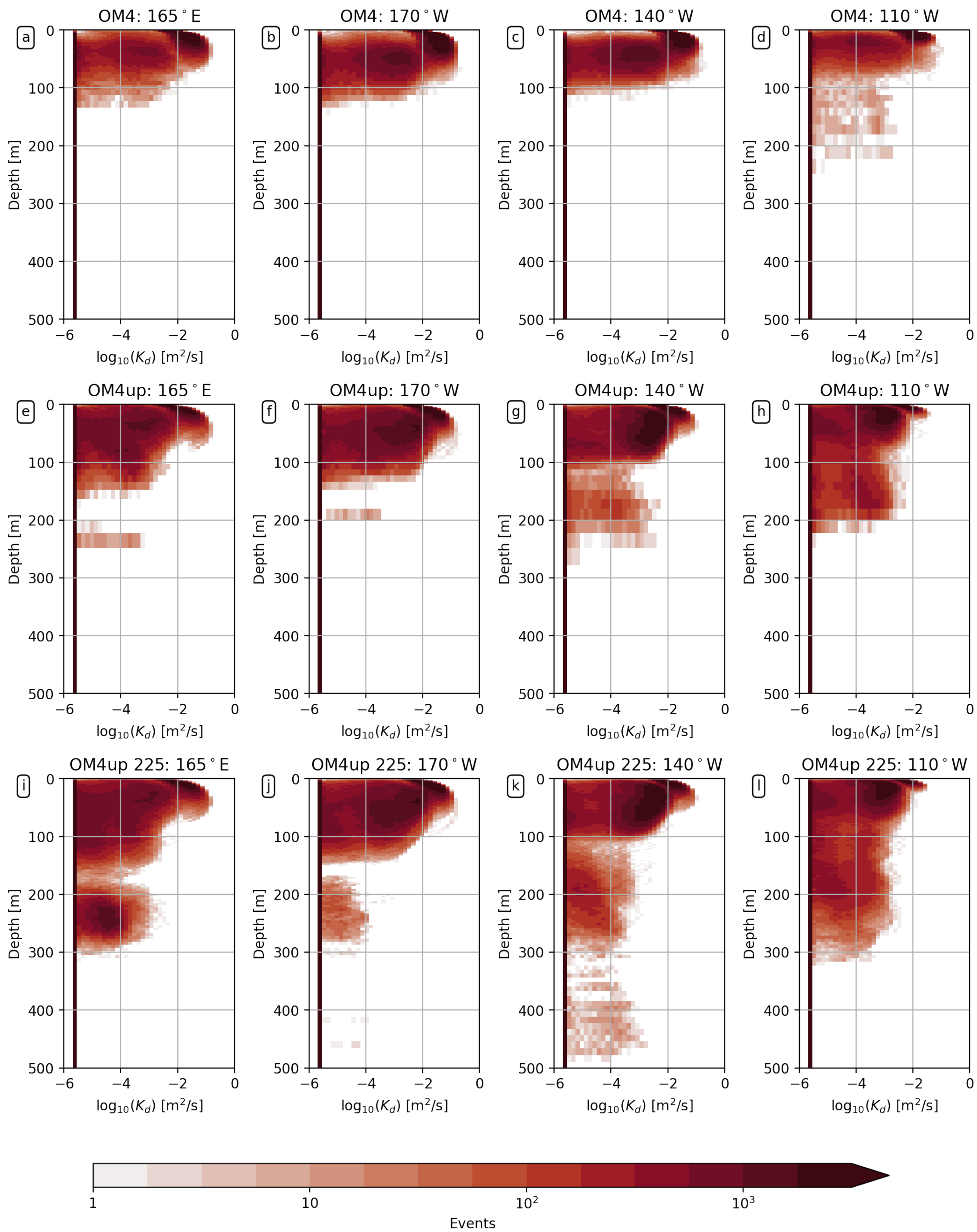

Figure 18. Discrete occurrence event heatmap for total vertical diffusivity in the OM4 model, the updated OM4 model, and the updated OM4 model with higher vertical resolution (225 levels).

tion sensitivity analysis. Our analysis also revealed significantly richer turbulence leading to potentially reduced biases in mixing and variability in OM4 with 225 layers over 75 layers. In future ocean model development it will be important to consider whether an increased number of vertical layers is required for simulating realistic turbulence and mixing or if parameterizations can be adapted for use with coarser vertical grids.

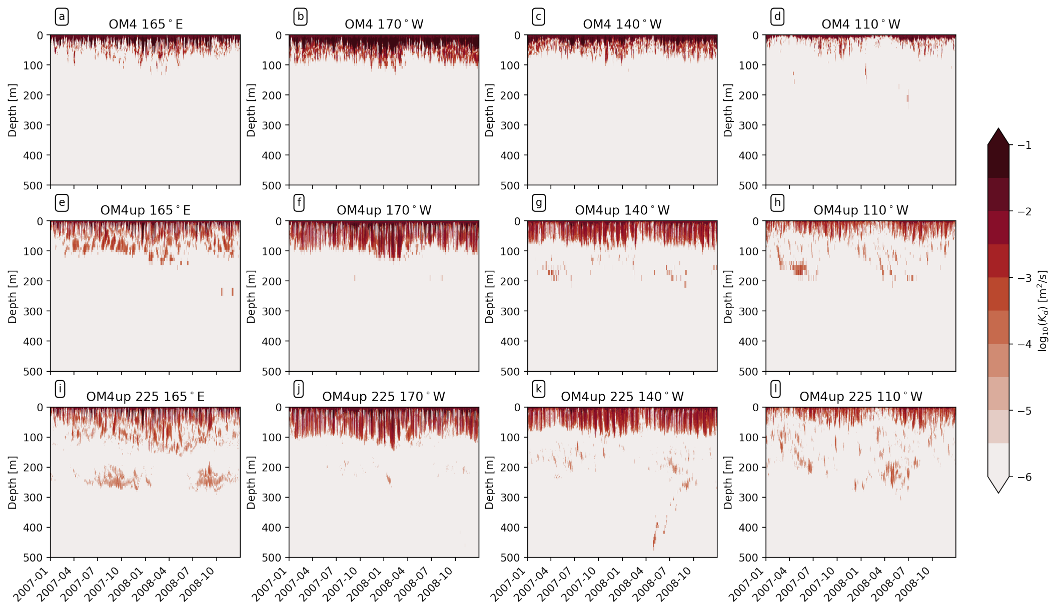

Figure 19. Comparison of total vertical diffusivity depth-time Hovmöller at same four TAO mooring longitudes discussed in detail of this paper for the OM4 model (upper), updated OM4 model (middle row), and 225 vertical level model (bottom row).

Future work will investigate the impacts of these improved mixing schemes in CGCMs to evaluate the hypothesis that the improvements in OM4 lead to improvements in tropical climate in a coupled climate model. Preliminary analysis of the OM4up changes in developmental CGCMs at GFDL (not including CM4) indicate that the improved diurnal cycle and eastern Pacific stratification are also found in the CGCMs. However, these preliminary results have not yet revealed any robust feedbacks to the atmospheric model. Those preliminary results also suggest that the atmospheric models and model coupling present challenges to improving the equatorial oceans, since outstanding issues in simulating tropical patterns of winds, precipitation, and clouds can degrade the response of the ocean model within the CGCM.

The present work demonstrates the utility of LES, the TAO network, and Argo floats for developing and evaluating OGCMs and CGCMs. The combination of long term and expansive datasets are a uniquely important tool for evaluating ocean climate model simulations, and should be combined with process based (e.g., LES) analysis methods to continue to evaluate and improve model biases.

6 Open Research

The source codes and model parameter settings needed for the SCM MOM6 experiments and the notebooks needed to generate the figures in this manuscript are available at `github.com/breichl/EqPac_Paper` (NOTE: this will be registered to Zenodo for publication). SCM and 3D processed output from MOM6 simulations is available at `dx.doi.org/10.5281/zenodo.10406424` (NOTE: this url will work if DOI not yet registered at time of review `https://zenodo.org/records/10406424`). LES and ROMS data for the column model simulations were obtained by following the instructions of Whitt et al. (2022). Raw Argo data was obtained from `dx.doi.org/10.17882/42182`, where the snapshot from July 2023 was used for this study. Gridded Argo data was obtained from `http://sioargo.ucsd.edu/RG_Climatology.html`. TAO data was obtained from `pmel.noaa.gov/gtmba/`.

Acknowledgments

A. A. was supported by Award NA18OAR4320123 from the National Oceanic and Atmospheric Administration, U.S. Department of Commerce. The statements, findings, conclusions, and recommendations are those of the author(s) and do not necessarily reflect the views of the National Oceanic and Atmospheric Administration, or the U.S. Department of Commerce. We are extremely grateful to the programs that support the TAO mooring operation and its maintenance, including the GTMBA Project Office of NOAA/PMEL. We are also indebted to the many efforts of the Argo program, which provides data that were collected and made freely available by the International Argo Program and the national programs that contribute to it (http://www.argo.ucsd.edu, http://argo.jcommops.org). The Argo Program is part of the Global Ocean Observing System. We thank Dr. Daniel Whitt for conversations related to this work and for making the LES experiments presented in Whitt et al. (2022) easy to download and use. We acknowledge use of the colormaps from the cmocean package (Thyng et al., 2016). We thank Feiyu Lu and Matthew Harrison for helpful comments during internal reviews of this manuscript.

Appendix A Table of acronyms and symbols

ADCP	Accoustic Doppler current profiler
CGCM	Coupled general circulation model
CM4	Global Climate Model 4
CMIP	Coupled Model Intercomparison Project 6
ENSO	El Niño / Southern Oscillation
ePBL	energetics-based planetary boundary layer
GFDL	Geophysical Fluid Dynamics Laboratory
JHL	Jackson et al. (2008) shear mixing
JRA55	Japanese 55-year Reanalysis
LES	Large eddy simulation
MLE	Mixed layer eddy parameterization
MOM6	Modular Ocean Model 6
OGCM	ocean general circulation model
OM4	Ocean and Sea-Ice Simulator 4
OMIP	Ocean Model Intercomparison Project
SIS2	Sea Ice Simulator 2
SST	Sea surface temperature
TAO	Tropical Atmosphere Ocean
TKE	Turbulent kinetic energy
N^2	Buoyancy frequency (Brunt-Väisälä)
S^2	Shear frequency
Ri	Richardson Number

Table A1. Commonly used acronyms and symbols in the paper.

References

Adcroft, A., Anderson, W., Balaji, V., Blanton, C., Bushuk, M., Dufour, C. O., ... Zhang, R. (2019). The GFDL Global Ocean and Sea Ice Model OM4.0: Model Description and Simulation Features. *Journal of Advances in Modeling Earth Systems*, *11*(10), 3167–3211. doi: 10.1029/2019MS001726

Arakawa, A., & Lamb, V. R. (1977). Computational Design of the Basic Dynamical Processes of the UCLA General Circulation Model. In *Methods in Computational Physics: Advances in Research and Applications* (Vol. 17, pp. 173–265). Elsevier. doi: 10.1016/B978-0-12-460817-7.50009-4

Argo. (2023). *Argo float data and metadata from Global Data Assembly Centre (Argo GDAC).* SEANOE. Retrieved from `https://www.seanoe.org/data/00311/42182/` doi: 10.17882/42182

Chang, Y.-S., Zhang, S., Rosati, A., Delworth, T. L., & Stern, W. F. (2013). An assessment of oceanic variability for 1960–2010 from the GFDL ensemble coupled data assimilation. *Climate Dynamics*, *40*(3-4), 775–803. doi: 10.1007/s00382-012-1412-2

Cherian, D. A., Whitt, D. B., Holmes, R. M., Lien, R.-C., Bachman, S. D., & Large, W. G. (2021). Off-Equatorial Deep-Cycle Turbulence Forced by Tropical Instability Waves in the Equatorial Pacific. *Journal of Physical Oceanography*, *51*(5), 1575–1593. doi: 10.1175/JPO-D-20-0229.1

Chiodi, A. M., & Harrison, D. E. (2017). Simulating ENSO SSTAs from TAO/TRITON Winds: The Impacts of 20 Years of Buoy Observations in the Pacific Waveguide and Comparison with Reanalysis Products. *Journal of Climate*, *30*(3), 1041–1059. doi: 10.1175/JCLI-D-15-0865.1

Delworth, T. L., Cooke, W. F., Adcroft, A., Bushuk, M., Chen, J., Dunne, K. A., . . . Zhao, M. (2020). SPEAR: The Next Generation GFDL Modeling System for Seasonal to Multidecadal Prediction and Projection. *Journal of Advances in Modeling Earth Systems*, *12*(3), e2019MS001895. doi: 10.1029/2019MS001895

Dunne, J. P., Horowitz, L. W., Adcroft, A. J., Ginoux, P., Held, I. M., John, J. G., . . . Zhao, M. (2020). The GFDL Earth System Model Version 4.1 (GFDL-ESM 4.1): Overall Coupled Model Description and Simulation Characteristics. *Journal of Advances in Modeling Earth Systems*, *12*(11). doi: 10.1029/2019MS002015

Eyring, V., Bony, S., Meehl, G. A., Senior, C. A., Stevens, B., Stouffer, R. J., & Taylor, K. E. (2016). Overview of the Coupled Model Intercomparison Project Phase 6 (CMIP6) experimental design and organization. *Geoscientific Model Development*, *9*(5), 1937–1958. doi: 10.5194/gmd-9-1937-2016

Farneti, R., Stiz, A., & Ssebandeke, J. B. (2022). Improvements and persistent biases in the southeast tropical Atlantic in CMIP models. *npj Climate and Atmospheric Science*, *5*(1), 42. doi: 10.1038/s41612-022-00264-4

Fox-Kemper, B., Danabasoglu, G., Ferrari, R., Griffies, S., Hallberg, R., Holland, M., . . . Samuels, B. (2011). Parameterization of mixed layer eddies. III: Implementation and impact in global ocean climate simulations. *Ocean Modelling*, *39*(1-2), 61–78. doi: 10.1016/j.ocemod.2010.09.002

Gnanadesikan, A., & Anderson, W. G. (2009). Ocean Water Clarity and the Ocean General Circulation in a Coupled Climate Model. *Journal of Physical Oceanography*, *39*(2), 314–332. doi: 10.1175/2008JPO3935.1

Gregg, M. C., Peters, H., Wesson, J. C., Oakey, N. S., & Shay, T. J. (1985). Intensive measurements of turbulence and shear in the equatorial undercurrent. *Nature*, *318*(6042), 140–144. doi: 10.1038/318140a0

Griffies, S. M., Danabasoglu, G., Durack, P. J., Adcroft, A. J., Balaji, V., Böning, C. W., . . . Yeager, S. G. (2016). OMIP contribution to CMIP6: experimental and diagnostic protocol for the physical component of the Ocean Model Intercomparison Project. *Geoscientific Model Development*, *9*(9), 3231–3296. doi: 10.5194/gmd-9-3231-2016

Griffies, S. M., & Hallberg, R. W. (2000). Biharmonic Friction with a Smagorinsky-Like Viscosity for Use in Large-Scale Eddy-Permitting Ocean Models. *Monthly Weather Review*, *128*(8), 2935–2946. doi: 10.1175/1520-0493(2000)128<2935:BFWASL>2.0.CO;2

Harrison, M. J., & Hallberg, R. W. (2008). Pacific Subtropical Cell Response to Reduced Equatorial Dissipation. *Journal of Physical Oceanography*, *38*(9), 1894–1912. doi: 10.1175/2008JPO3708.1

Hawkins, E., & Sutton, R. (2009). The Potential to Narrow Uncertainty in Regional Climate Predictions. *Bulletin of the American Meteorological Society*, *90*(8), 1095–1108. doi: 10.1175/2009BAMS2607.1

Held, I. M., Guo, H., Adcroft, A., Dunne, J. P., Horowitz, L. W., Krasting, J., . . . Zadeh, N. (2019). Structure and Performance of GFDL's CM4.0 Climate Model. *Journal of Ad-*

vances in Modeling Earth Systems, *11*(11), 3691–3727. doi: 10.1029/2019MS001829
Holmes, R. M., & Thomas, L. N. (2015). The Modulation of Equatorial Turbulence by Tropical Instability Waves in a Regional Ocean Model. *Journal of Physical Oceanography*, *45*(4), 1155–1173. doi: 10.1175/JPO-D-14-0209.1
IPCC. (2021). *Climate change 2021: The physical science basis. contribution of working group i to the sixth assessment report of the intergovernmental panel on climate change* (Vol. In Press) [Book]. Cambridge, United Kingdom and New York, NY, USA: Cambridge University Press. doi: 10.1017/9781009157896
Jackson, L., Hallberg, R., & Legg, S. (2008). A Parameterization of Shear-Driven Turbulence for Ocean Climate Models. *Journal of Physical Oceanography*, *38*(5), 1033–1053. doi: 10.1175/2007JPO3779.1
Jia, Y., Richards, K. J., & Annamalai, H. (2021). The impact of vertical resolution in reducing biases in sea surface temperature in a tropical Pacific Ocean model. *Ocean Modelling*, *157*, 101722. doi: 10.1016/j.ocemod.2020.101722
Kessler, W. S. (2006). The circulation of the eastern tropical Pacific: A review. *Progress in Oceanography*, *69*(2-4), 181–217. doi: 10.1016/j.pocean.2006.03.009
Large, W. G., & Gent, P. R. (1999). Validation of Vertical Mixing in an Equatorial Ocean Model Using Large Eddy Simulations and Observations. *Journal of Physical Oceanography*, *29*(3), 449–464. doi: 10.1175/1520-0485(1999)029<0449:VOVMIA>2.0.CO;2
Large, W. G., McWilliams, J. C., & Doney, S. C. (1994). Oceanic vertical mixing: A review and a model with a nonlocal boundary layer parameterization. *Reviews of Geophysics*, *32*(4), 363. doi: 10.1029/94RG01872
Li, G., & Xie, S.-P. (2012). Origins of tropical-wide SST biases in CMIP multi-model ensembles: TROPICAL-WIDE SST BIASES IN MODELS. *Geophysical Research Letters*, *39*(22), n/a–n/a. doi: 10.1029/2012GL053777
Li, G., & Xie, S.-P. (2014). Tropical Biases in CMIP5 Multimodel Ensemble: The Excessive Equatorial Pacific Cold Tongue and Double ITCZ Problems*. *Journal of Climate*, *27*(4), 1765–1780. doi: 10.1175/JCLI-D-13-00337.1
Li, Q., Reichl, B. G., Fox-Kemper, B., Adcroft, A. J., Belcher, S. E., Danabasoglu, G., ... Zheng, Z. (2019). Comparing Ocean Surface Boundary Vertical Mixing Schemes Including Langmuir Turbulence. *Journal of Advances in Modeling Earth Systems*, *11*(11), 3545–3592. doi: 10.1029/2019MS001810
Li, X., Cai, W., Meehl, G. A., Chen, D., Yuan, X., Raphael, M., ... Song, C. (2021). Tropical teleconnection impacts on Antarctic climate changes. *Nature Reviews Earth & Environment*, *2*(10), 680–698. doi: 10.1038/s43017-021-00204-5
L'Heureux, M. L., Tippett, M. K., & Barnston, A. G. (2015). Characterizing ENSO Coupled Variability and Its Impact on North American Seasonal Precipitation and Temperature*. *Journal of Climate*, *28*(10), 4231–4245. doi: 10.1175/JCLI-D-14-00508.1
Manizza, M. (2005). Bio-optical feedbacks among phytoplankton, upper ocean physics and sea-ice in a global model. *Geophysical Research Letters*, *32*(5), L05603. doi: 10.1029/2004GL020778
McPhaden, M. J., Santoso, A., & Cai, W. (Eds.). (2020). *El niño southern oscillation in a changing climate* (Vol. 253) [Book]. Washington, DC: Wiley. doi: 10.1002/9781119548164
Meehl, G. A., Gent, P. R., Arblaster, J. M., Otto-Bliesner, B. L., Brady, E. C., & Craig, A. (2001). Factors that affect the amplitude of El Nino in global coupled climate models:. *Climate Dynamics*, *17*(7), 515–526. doi: 10.1007/PL00007929
Moum, J. N., & Caldwell, D. R. (1985). Local Influences on Shear-Flow Turbulence in the Equatorial Ocean. *Science*, *230*(4723), 315–316. doi: 10.1126/science.230.4723.315
Moum, J. N., Hughes, K. G., Shroyer, E. L., Smyth, W. D., Cherian, D., Warner, S. J., ... Dengler, M. (2022). Deep Cycle Turbulence in Atlantic and Pacific Cold Tongues. *Geophysical Research Letters*, *49*(8). doi: 10.1029/2021GL097345
Moum, J. N., Nash, J. D., & Smyth, W. D. (2011). Narrowband Oscillations in the Upper Equatorial Ocean. Part I: Interpretation as Shear Instabilities. *Journal of Physical*

Oceanography, *41*(3), 397–411. doi: 10.1175/2010JPO4450.1

Moum, J. N., Perlin, A., Nash, J. D., & McPhaden, M. J. (2013). Seasonal sea surface cooling in the equatorial Pacific cold tongue controlled by ocean mixing. *Nature*, *500*(7460), 64–67. doi: 10.1038/nature12363

Palmer, T., Shutts, G., Hagedorn, R., Doblas-Reyes, F., Jung, T., & Leutbecher, M. (2005). Representing model uncertainty in weather and climate prediction. *Annual Review of Earth and Planetary Sciences*, *33*(1), 163–193. doi: 10.1146/annurev.earth.33.092203.122552

Pei, S., Shinoda, T., Wang, W., & Lien, R. (2020). Simulation of Deep Cycle Turbulence by a Global Ocean General Circulation Model. *Geophysical Research Letters*, *47*(15). doi: 10.1029/2020GL088384

Peters, H., Gregg, M. C., & Sanford, T. B. (1994). The diurnal cycle of the upper equatorial ocean: Turbulence, fine-scale shear, and mean shear. *Journal of Geophysical Research*, *99*(C4), 7707. doi: 10.1029/93JC03506

Pham, H. T., Sarkar, S., & Winters, K. B. (2013). Large-Eddy Simulation of Deep-Cycle Turbulence in an Equatorial Undercurrent Model. *Journal of Physical Oceanography*, *43*(11), 2490–2502. doi: 10.1175/JPO-D-13-016.1

Pujiana, K., Moum, J. N., & Smyth, W. D. (2018). The Role of Turbulence in Redistributing Upper-Ocean Heat, Freshwater, and Momentum in Response to the MJO in the Equatorial Indian Ocean. *Journal of Physical Oceanography*, *48*(1), 197–220. doi: 10.1175/JPO-D-17-0146.1

Reichl, B. G., & Hallberg, R. (2018). A simplified energetics based planetary boundary layer (ePBL) approach for ocean climate simulations. *Ocean Modelling*, *132*, 112–129. doi: 10.1016/j.ocemod.2018.10.004

Richards, K. J., Xie, S.-P., & Miyama, T. (2009). Vertical mixing in the ocean and its impact on the coupled ocean–atmosphere system in the eastern tropical pacific. *Journal of Climate*, *22*(13), 3703 - 3719. doi: https://doi.org/10.1175/2009JCLI2702.1

Roemmich, D., & Gilson, J. (2009). The 2004–2008 mean and annual cycle of temperature, salinity, and steric height in the global ocean from the Argo Program. *Progress in Oceanography*, *82*(2), 81–100. doi: 10.1016/j.pocean.2009.03.004

Ropelewski, C. F., & Halpert, M. S. (1987). Global and Regional Scale Precipitation Patterns Associated with the El Niño/Southern Oscillation. *Monthly Weather Review*, *115*(8), 1606–1626. doi: 10.1175/1520-0493(1987)115<1606:GARSPP>2.0.CO;2

Smyth, W. D., & Moum, J. N. (2013). Marginal instability and deep cycle turbulence in the eastern equatorial Pacific Ocean. *Geophysical Research Letters*, *40*(23), 6181–6185. doi: 10.1002/2013GL058403

Smyth, W. D., Moum, J. N., Li, L., & Thorpe, S. A. (2013). Diurnal Shear Instability, the Descent of the Surface Shear Layer, and the Deep Cycle of Equatorial Turbulence. *Journal of Physical Oceanography*, *43*(11), 2432–2455. doi: 10.1175/JPO-D-13-089.1

Stramma, L., Johnson, G. C., Firing, E., & Schmidtko, S. (2010). Eastern Pacific oxygen minimum zones: Supply paths and multidecadal changes. *Journal of Geophysical Research: Oceans*, *115*(C9), 2009JC005976. doi: 10.1029/2009JC005976

Sun, C., Smyth, W. D., & Moum, J. N. (1998). Dynamic instability of stratified shear flow in the upper equatorial Pacific. *Journal of Geophysical Research: Oceans*, *103*(C5), 10323–10337. doi: 10.1029/98JC00191

Sun, Z., Liu, H., Lin, P., Tseng, Y., Small, J., & Bryan, F. (2019). The Modeling of the North Equatorial Countercurrent in the Community Earth System Model and its Oceanic Component. *Journal of Advances in Modeling Earth Systems*, *11*(2), 531–544. doi: 10.1029/2018MS001521

Taboada, F. G., Stock, C. A., Griffies, S. M., Dunne, J., John, J. G., Small, R. J., & Tsujino, H. (2019). Surface winds from atmospheric reanalysis lead to contrasting oceanic forcing and coastal upwelling patterns. *Ocean Modelling*, *133*, 79–111. doi: 10.1016/j.ocemod.2018.11.003

Thyng, K., Greene, C., Hetland, R., Zimmerle, H., & DiMarco, S. (2016). True Colors of

Oceanography: Guidelines for Effective and Accurate Colormap Selection. *Oceanography*, *29*(3), 9–13. doi: 10.5670/oceanog.2016.66

Trenberth, K. E., Branstator, G. W., Karoly, D., Kumar, A., Lau, N.-C., & Ropelewski, C. (1998). Progress during TOGA in understanding and modeling global teleconnections associated with tropical sea surface temperatures. *Journal of Geophysical Research: Oceans*, *103*(C7), 14291–14324. doi: 10.1029/97JC01444

Tsujino, H., Urakawa, L. S., Griffies, S. M., Danabasoglu, G., Adcroft, A. J., Amaral, A. E., . . . Yu, Z. (2020). Evaluation of global ocean–sea-ice model simulations based on the experimental protocols of the Ocean Model Intercomparison Project phase 2 (OMIP-2). *Geoscientific Model Development*, *13*(8), 3643–3708. doi: 10.5194/gmd-13-3643-2020

Tsujino, H., Urakawa, S., Nakano, H., Small, R. J., Kim, W. M., Yeager, S. G., . . . Yamazaki, D. (2018). JRA-55 based surface dataset for driving ocean–sea-ice models (JRA55-do). *Ocean Modelling*, *130*, 79–139. doi: 10.1016/j.ocemod.2018.07.002

Umlauf, L., & Burchard, H. (2003). A generic length-scale equation for geophysical turbulence models. *Journal of Marine Research*, *61*(2), 235–265. doi: 10.1357/002224003322005087

Voldoire, A., Exarchou, E., Sanchez-Gomez, E., Demissie, T., Deppenmeier, A.-L., Frauen, C., . . . Traoré, A.-K. (2019). Role of wind stress in driving SST biases in the Tropical Atlantic. *Climate Dynamics*, *53*(5-6), 3481–3504. doi: 10.1007/s00382-019-04717-0

Wang, D., Large, W. G., & McWilliams, J. C. (1996). Large-eddy simulation of the equatorial ocean boundary layer: Diurnal cycling, eddy viscosity, and horizontal rotation. *Journal of Geophysical Research: Oceans*, *101*(C2), 3649–3662. doi: 10.1029/95JC03441

Wang, D., McWilliams, J. C., & Large, W. G. (1998). Large-Eddy Simulation of the Diurnal Cycle of Deep Equatorial Turbulence. *Journal of Physical Oceanography*, *28*(1), 129–148. doi: 10.1175/1520-0485(1998)028<0129:LESOTD>2.0.CO;2

Whitt, D. B., Cherian, D. A., Holmes, R. M., Bachman, S. D., Lien, R.-C., Large, W. G., & Moum, J. N. (2022). Simulation and Scaling of the Turbulent Vertical Heat Transport and Deep-Cycle Turbulence across the Equatorial Pacific Cold Tongue. *Journal of Physical Oceanography*, *52*(5), 981–1014. doi: 10.1175/JPO-D-21-0153.1

Figure.

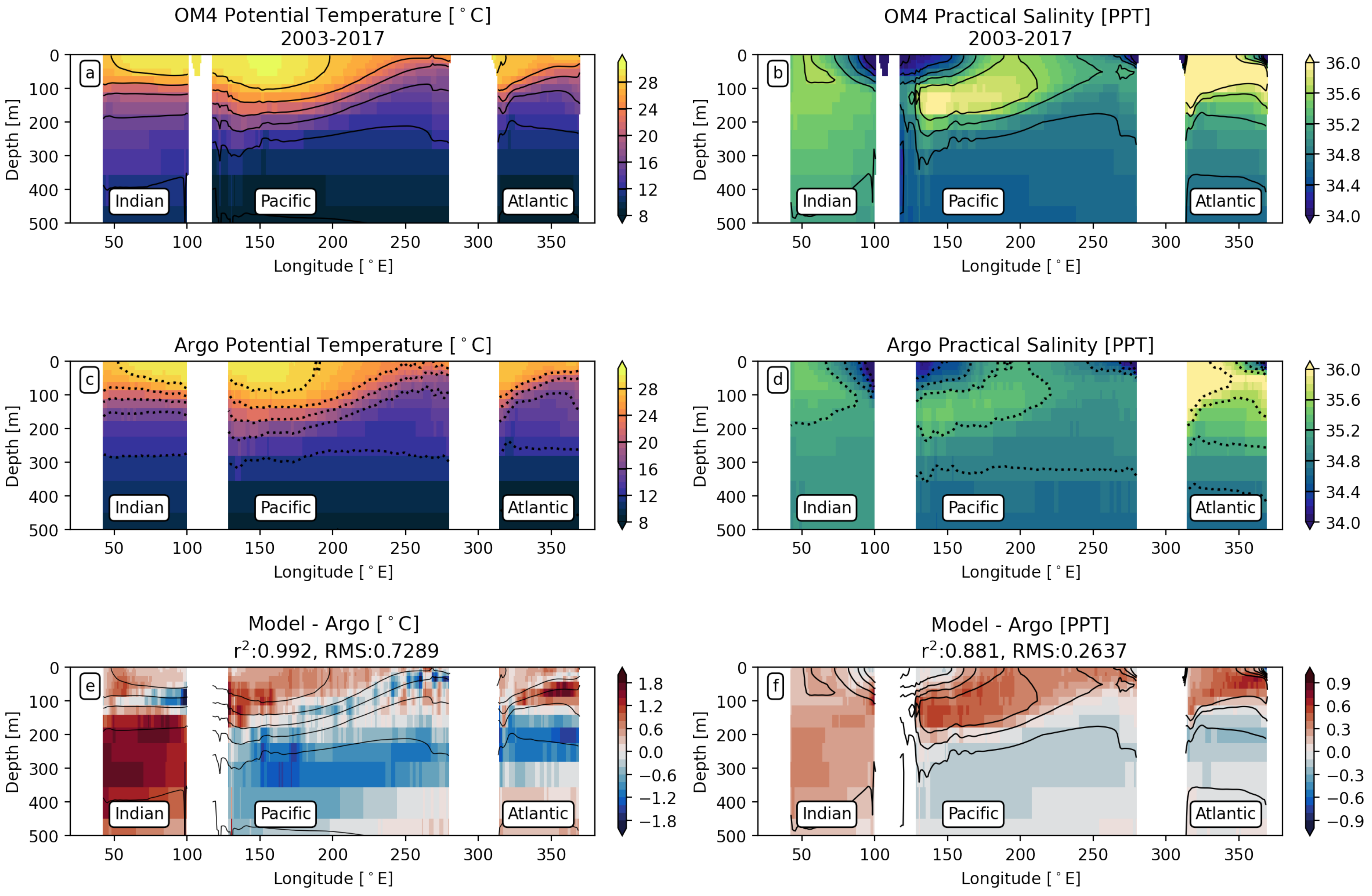

OM4 Potential Temperature [$^\circ$C]
2003-2017
OM4 Practical Salinity [PPT]
2003-2017
Argo Potential Temperature [$^\circ$C]
Argo Practical Salinity [PPT]
Model - Argo [$^\circ$C]
r^2:0.992, RMS:0.7289
Model - Argo [PPT]
r^2:0.881, RMS:0.2637
a
b
c
d
e
f
Indian
Pacific
Atlantic
Depth [m]
Longitude [$^\circ$E]

Figure.

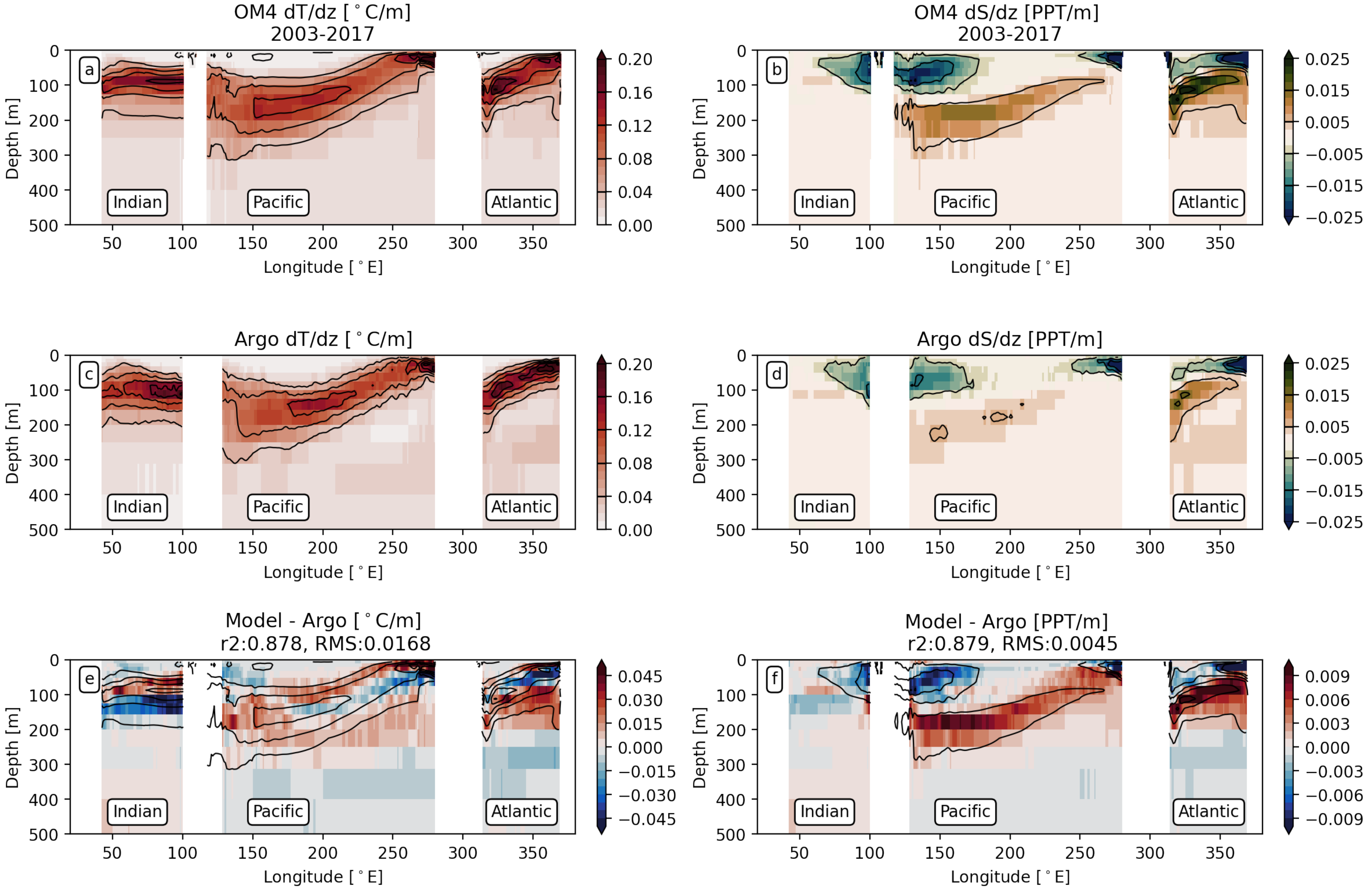

OM4 dT/dz [$^\circ$C/m]
2003-2017
OM4 dS/dz [PPT/m]
2003-2017
Argo dT/dz [$^\circ$C/m]
Argo dS/dz [PPT/m]
Model - Argo [$^\circ$C/m]
r2:0.878, RMS:0.0168
Model - Argo [PPT/m]
r2:0.879, RMS:0.0045
a
b
c
d
e
f
Indian
Pacific
Atlantic
Depth [m]
Longitude [$^\circ$E]

Figure.

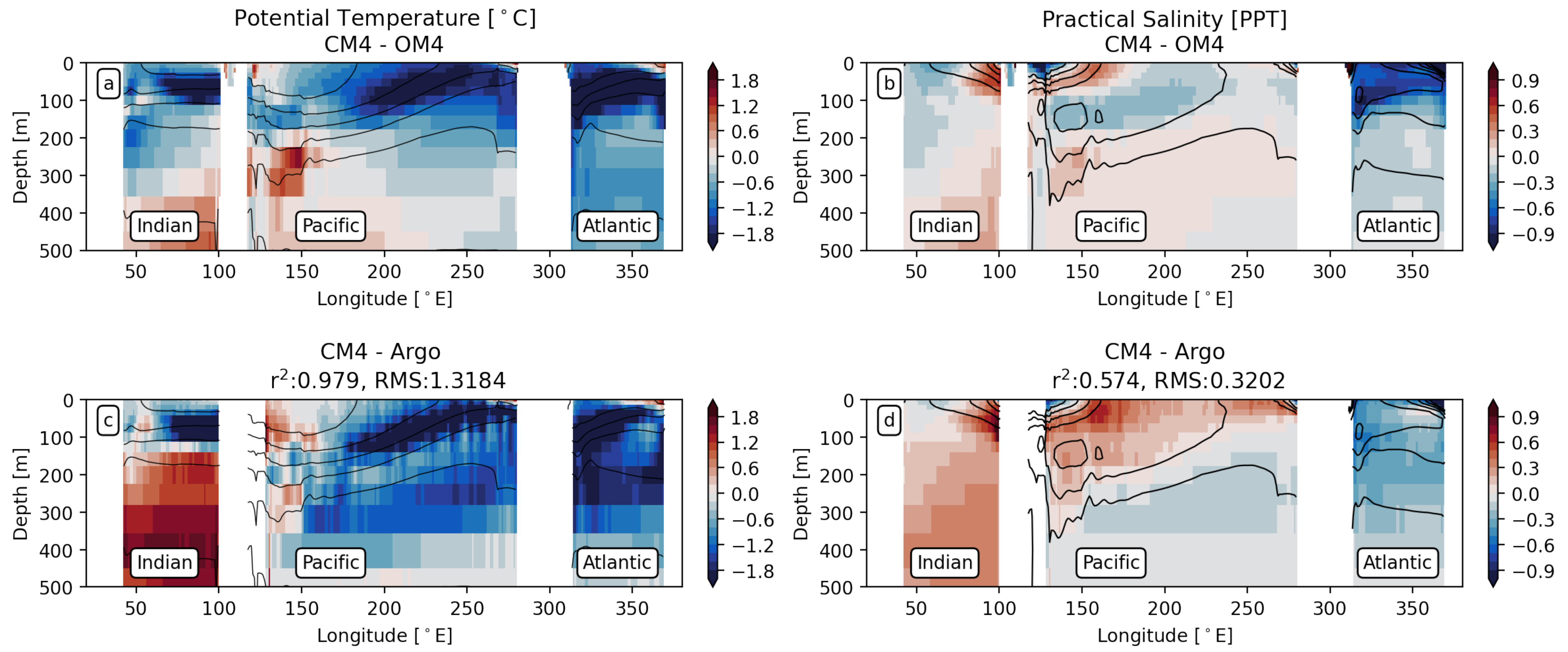

Potential Temperature [°C]
CM4 - OM4
Practical Salinity [PPT]
CM4 - OM4
CM4 - Argo
r2:0.979, RMS:1.3184
CM4 - Argo
r2:0.574, RMS:0.3202
a
b
c
d
Indian
Pacific
Atlantic
Depth [m]
Longitude [°E]

Figure.

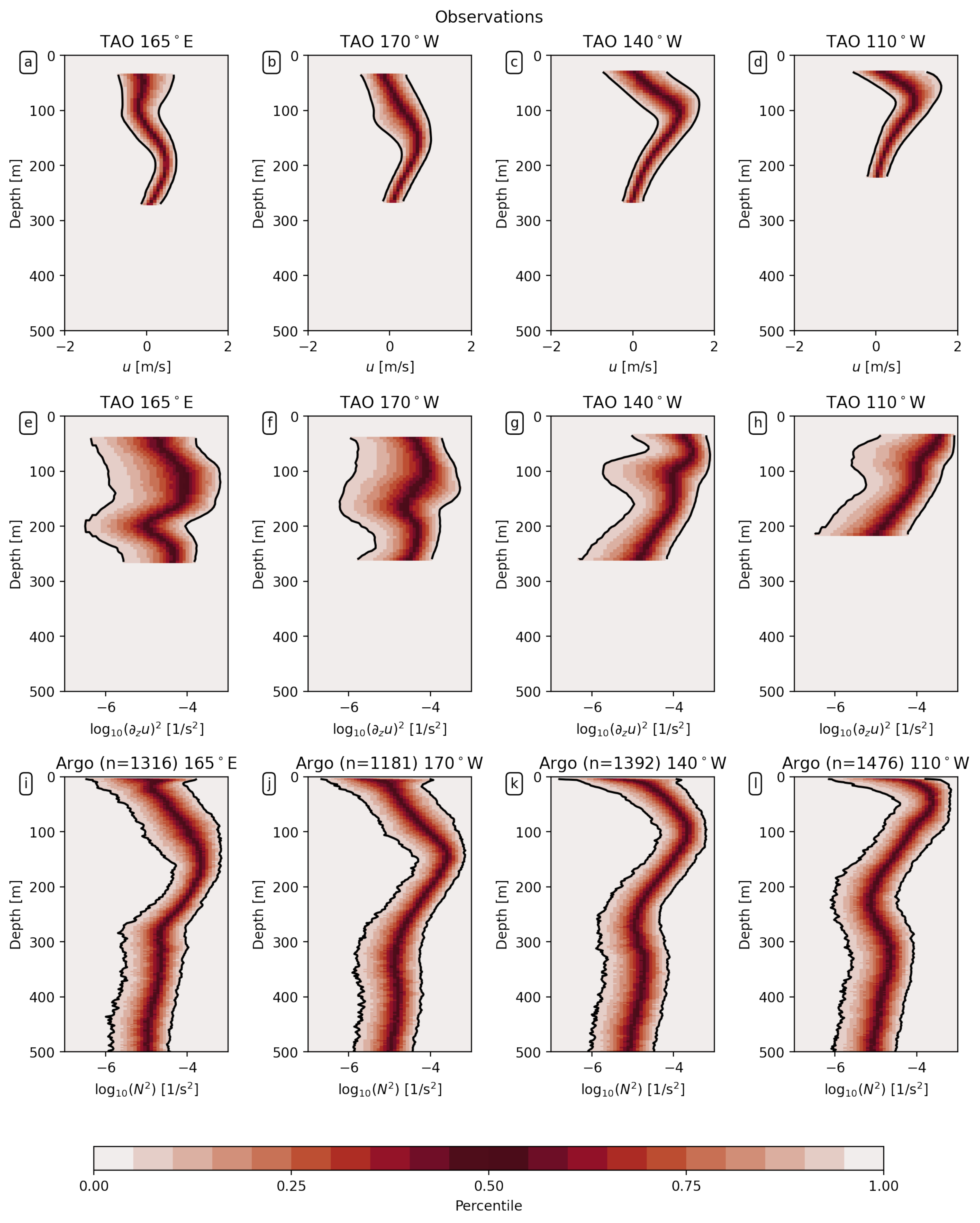

Observations
TAO 165°E
TAO 170°W
TAO 140°W
TAO 110°W
a
b
c
d
Depth [m]
u [m/s]
e
f
g
h
$\log_{10}(\partial_z u)^2$ [1/s^2]
Argo (n=1316) 165°E
Argo (n=1181) 170°W
Argo (n=1392) 140°W
Argo (n=1476) 110°W
i
j
k
l
$\log_{10}(N^2)$ [1/s^2]
Percentile
0.00
0.25
0.50
0.75
1.00

Figure.

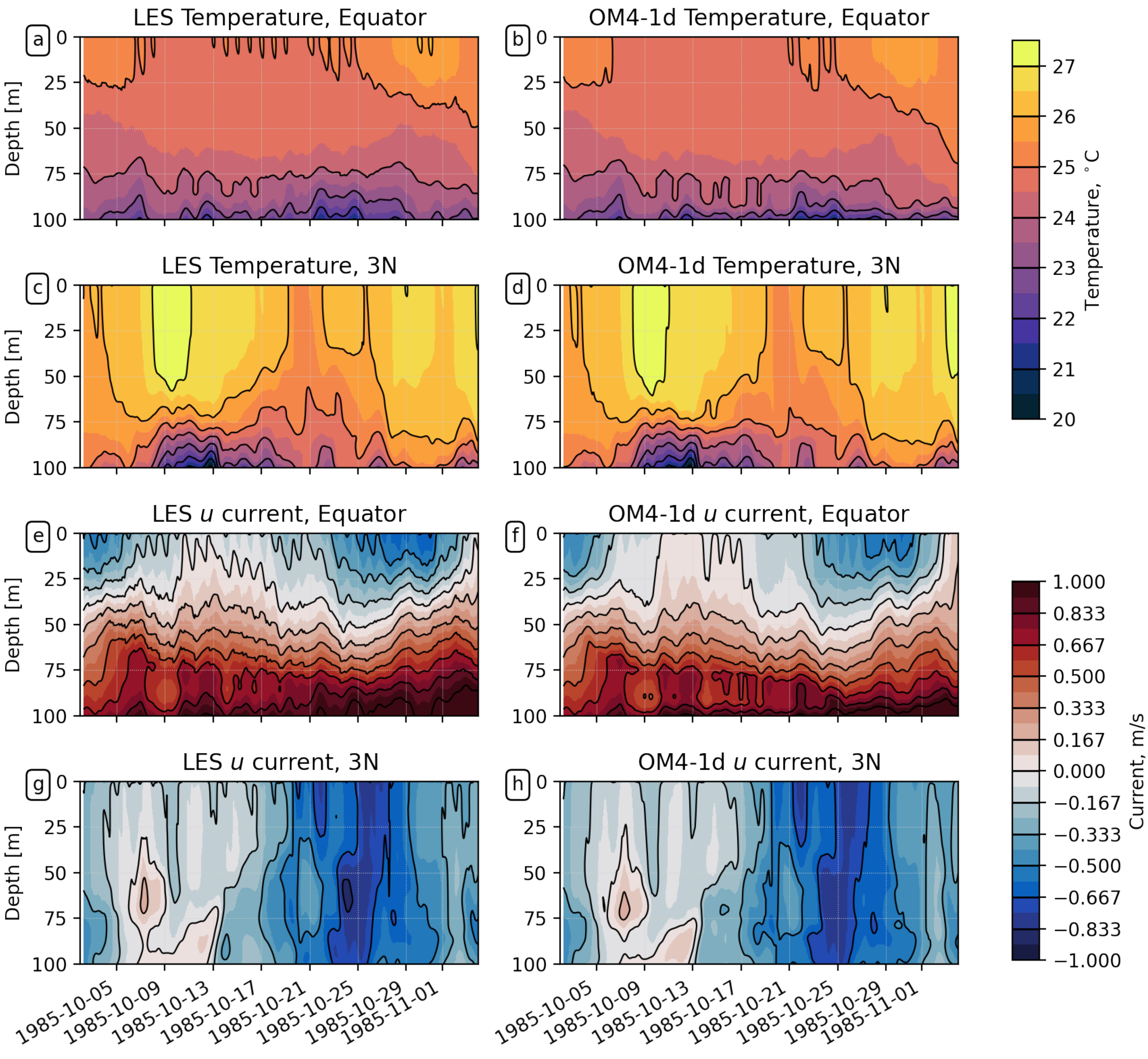

LES Temperature, Equator
OM4-1d Temperature, Equator
LES Temperature, 3N
OM4-1d Temperature, 3N
LES u current, Equator
OM4-1d u current, Equator
LES u current, 3N
OM4-1d u current, 3N
a
b
c
d
e
f
g
h
Depth [m]
0
25
50
75
100
Temperature, °C
20
21
22
23
24
25
26
27
Current, m/s
1.000
0.833
0.667
0.500
0.333
0.167
0.000
−0.167
−0.333
−0.500
−0.667
−0.833
−1.000
1985-10-05
1985-10-09
1985-10-13
1985-10-17
1985-10-21
1985-10-25
1985-10-29
1985-11-01

Figure.

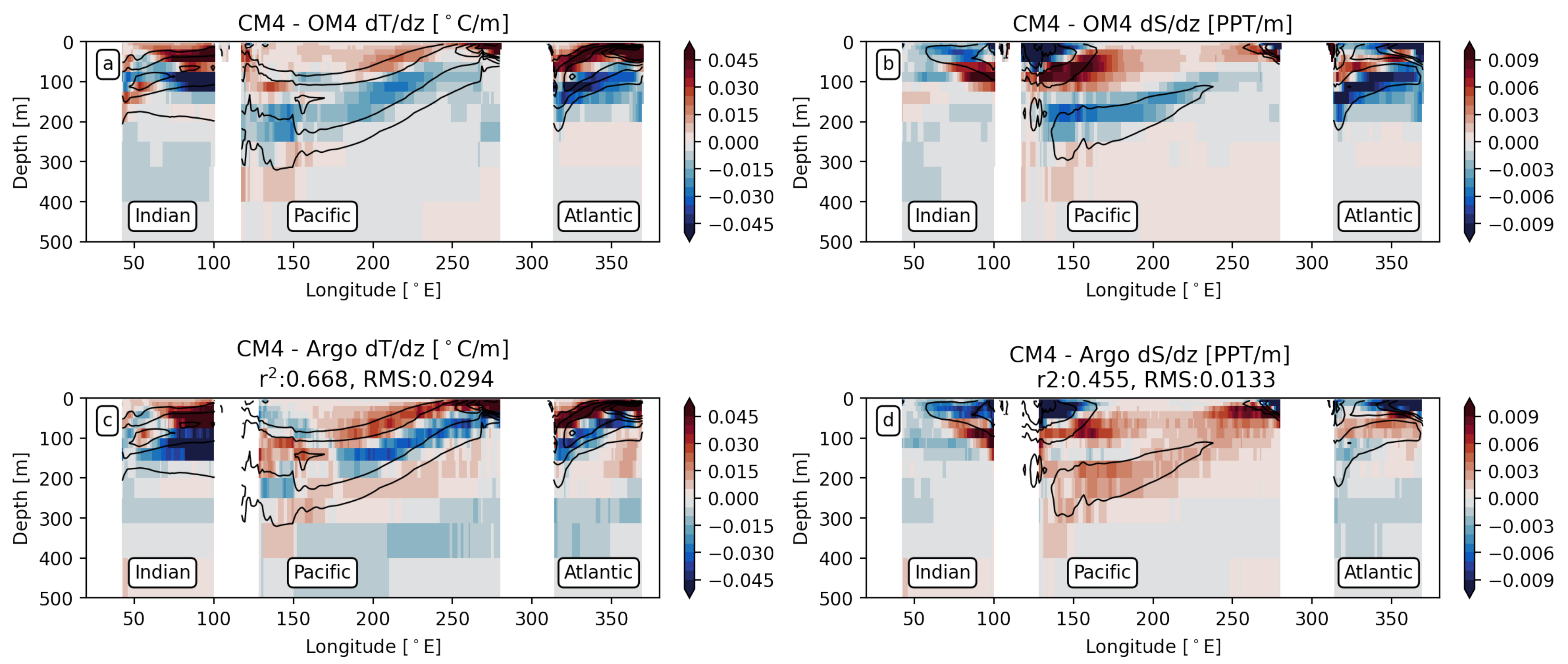
CM4 - OM4 dT/dz [$^\circ$C/m]
CM4 - OM4 dS/dz [PPT/m]
CM4 - Argo dT/dz [$^\circ$C/m]
r^2:0.668, RMS:0.0294
CM4 - Argo dS/dz [PPT/m]
r2:0.455, RMS:0.0133
a
b
c
d
Depth [m]
Longitude [$^\circ$E]
Indian
Pacific
Atlantic

Figure.

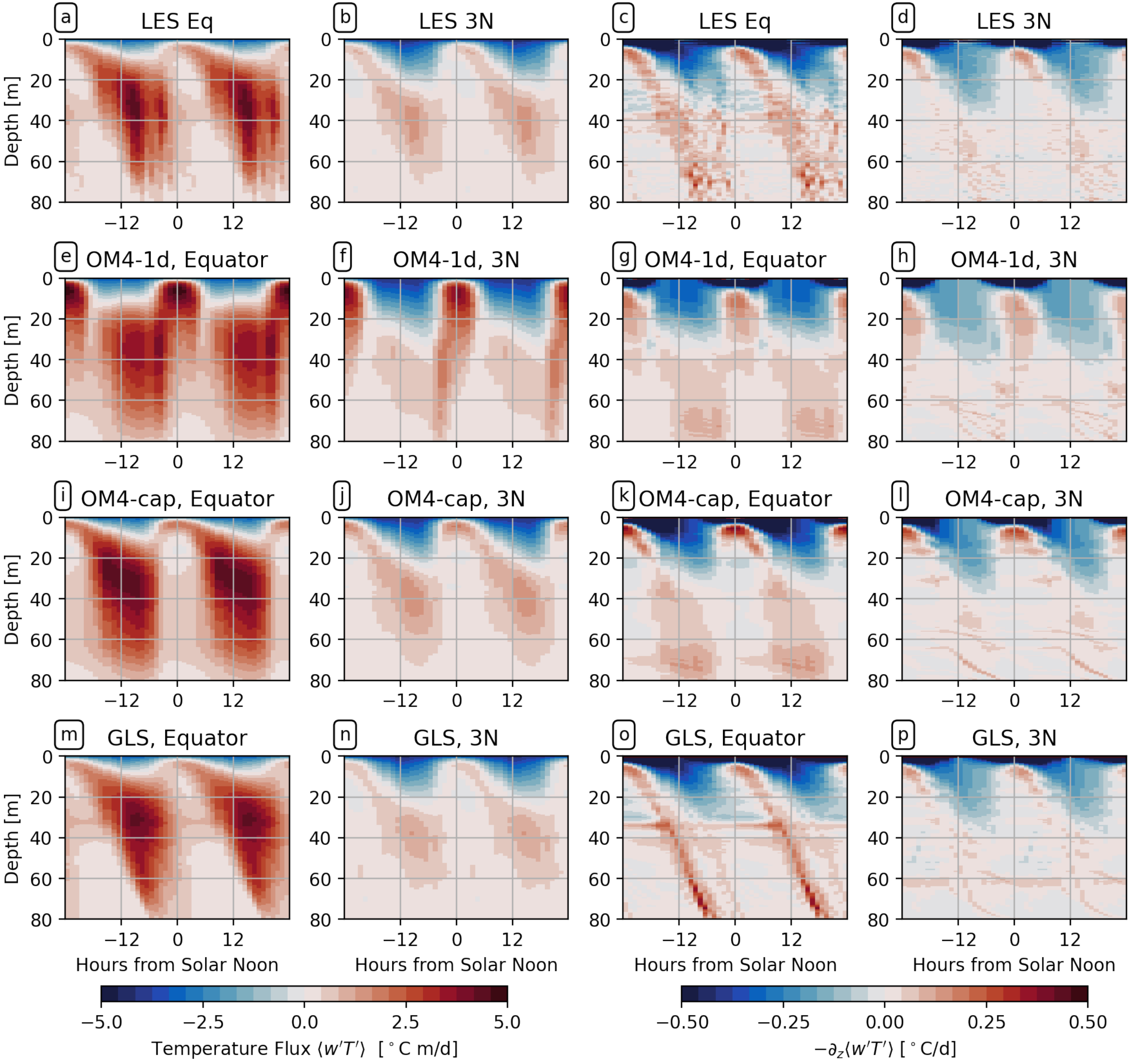

a LES Eq
b LES 3N
c LES Eq
d LES 3N
e OM4-1d, Equator
f OM4-1d, 3N
g OM4-1d, Equator
h OM4-1d, 3N
i OM4-cap, Equator
j OM4-cap, 3N
k OM4-cap, Equator
l OM4-cap, 3N
m GLS, Equator
n GLS, 3N
o GLS, Equator
p GLS, 3N
Depth [m]
0
20
40
60
80
−12
0
12
Hours from Solar Noon
−5.0
−2.5
0.0
2.5
5.0
Temperature Flux ⟨w′T′⟩ [°C m/d]
−0.50
−0.25
0.00
0.25
0.50
−∂z⟨w′T′⟩ [°C/d]

Figure.

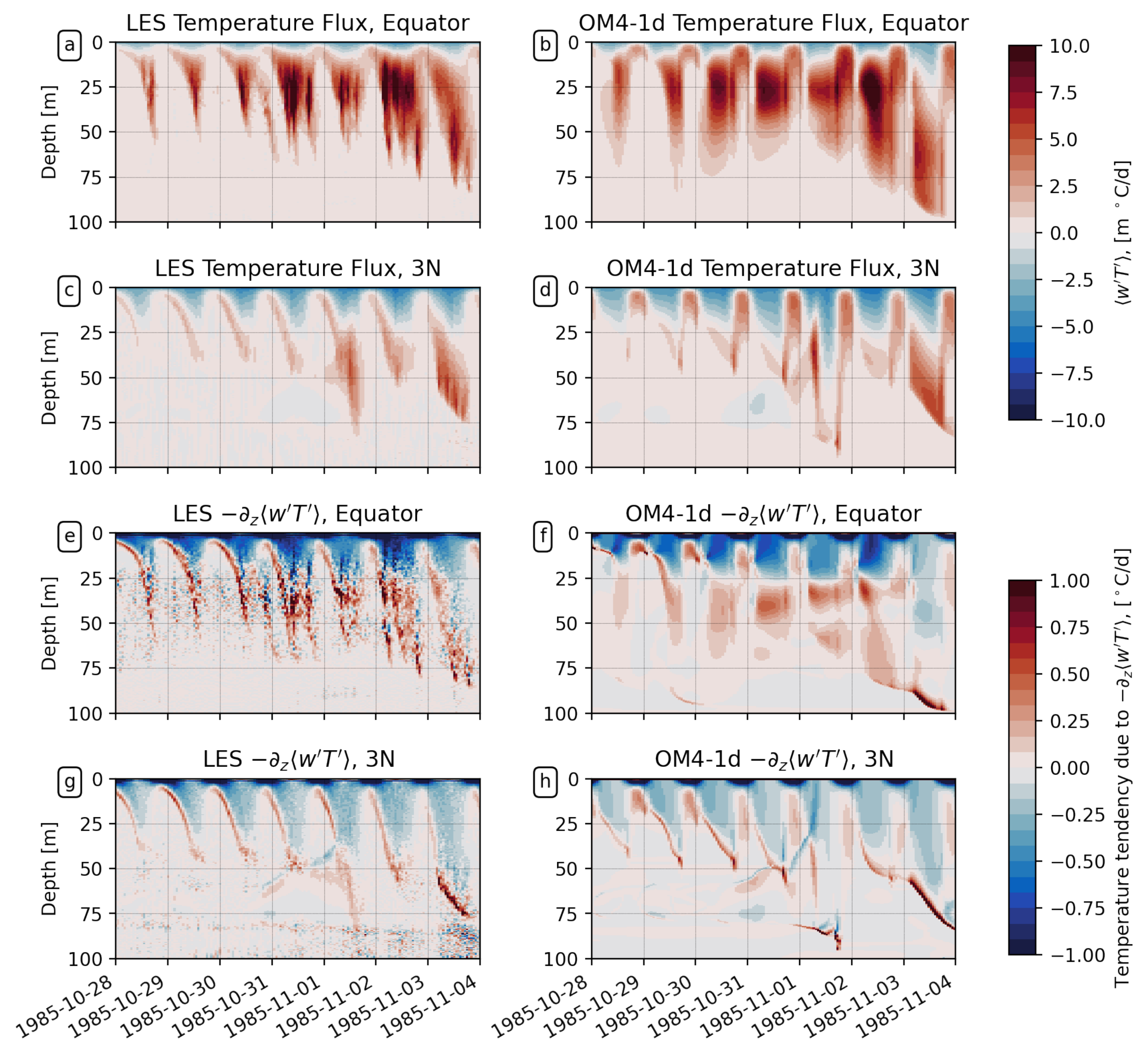
LES Temperature Flux, Equator
OM4-1d Temperature Flux, Equator
LES Temperature Flux, 3N
OM4-1d Temperature Flux, 3N
LES $-\partial_z\langle w'T'\rangle$, Equator
OM4-1d $-\partial_z\langle w'T'\rangle$, Equator
LES $-\partial_z\langle w'T'\rangle$, 3N
OM4-1d $-\partial_z\langle w'T'\rangle$, 3N
a
b
c
d
e
f
g
h
Depth [m]
0
25
50
75
100
1985-10-28
1985-10-29
1985-10-30
1985-10-31
1985-11-01
1985-11-02
1985-11-03
1985-11-04
$\langle w'T'\rangle$, [m $^\circ$C/d]
10.0
7.5
5.0
2.5
0.0
−2.5
−5.0
−7.5
−10.0
Temperature tendency due to $-\partial_z\langle w'T'\rangle$, [$^\circ$C/d]
1.00
0.75
0.50
0.25
0.00
−0.25
−0.50
−0.75
−1.00

Figure.

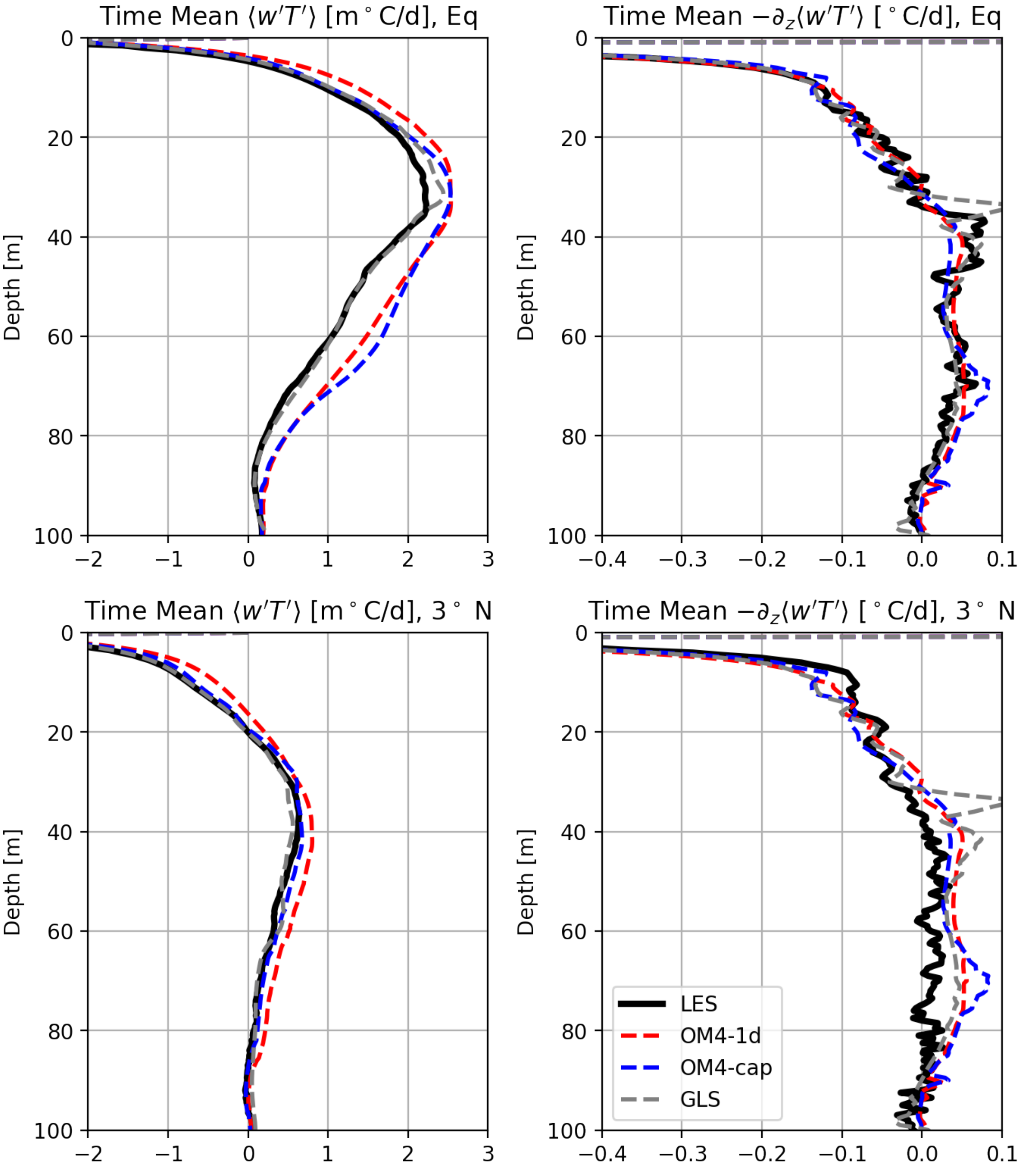

Time Mean $\langle w'T' \rangle$ [m$^\circ$C/d], Eq
Time Mean $-\partial_z \langle w'T' \rangle$ [$^\circ$C/d], Eq
Time Mean $\langle w'T' \rangle$ [m$^\circ$C/d], 3° N
Time Mean $-\partial_z \langle w'T' \rangle$ [$^\circ$C/d], 3° N
Depth [m]
0
20
40
60
80
100
−2
−1
0
1
2
3
−0.4
−0.3
−0.2
−0.1
0.0
0.1
LES
OM4-1d
OM4-cap
GLS

Figure.

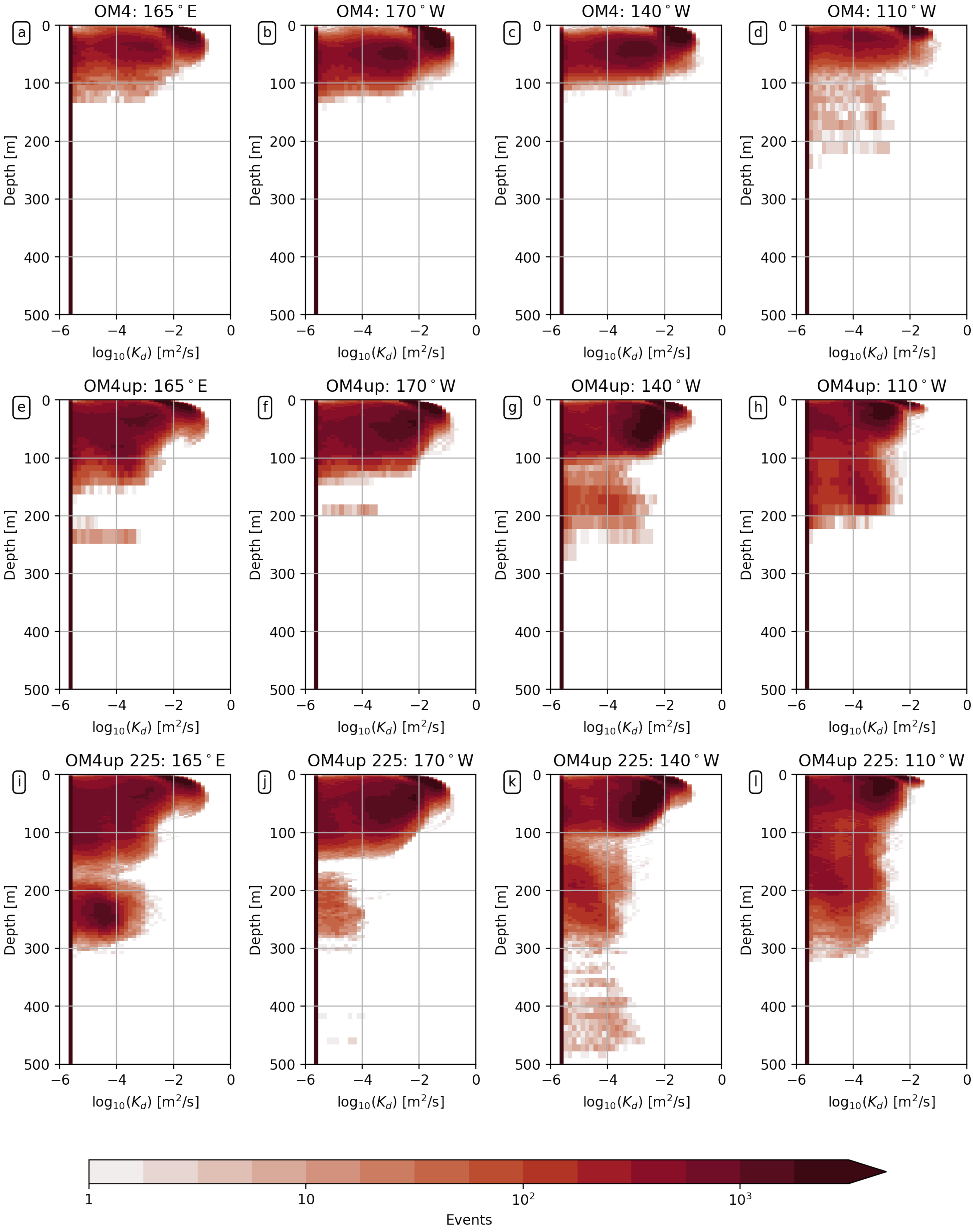
OM4: 165°E
OM4: 170°W
OM4: 140°W
OM4: 110°W
OM4up: 165°E
OM4up: 170°W
OM4up: 140°W
OM4up: 110°W
OM4up 225: 165°E
OM4up 225: 170°W
OM4up 225: 140°W
OM4up 225: 110°W
a
b
c
d
e
f
g
h
i
j
k
l
Depth [m]
0
100
200
300
400
500
$\log_{10}(K_d)$ [m^2/s]
−6
−4
−2
0
1
10
10^2
10^3
Events

Figure.

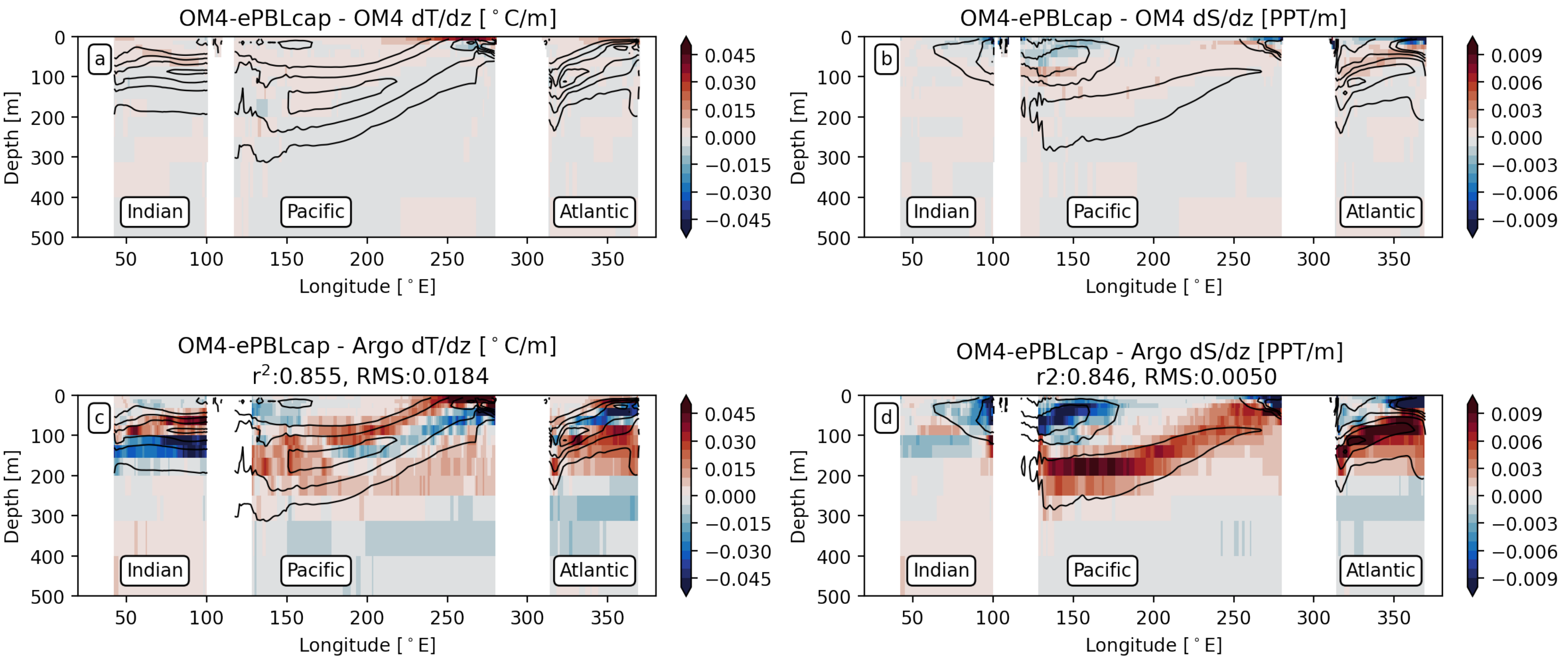

OM4-ePBLcap - OM4 dT/dz [$^\circ$C/m]
OM4-ePBLcap - OM4 dS/dz [PPT/m]
OM4-ePBLcap - Argo dT/dz [$^\circ$C/m]
r^2:0.855, RMS:0.0184
OM4-ePBLcap - Argo dS/dz [PPT/m]
r2:0.846, RMS:0.0050
a
b
c
d
Indian
Pacific
Atlantic
Depth [m]
Longitude [$^\circ$E]
0
100
200
300
400
500
50
100
150
200
250
300
350
0.045
0.030
0.015
0.000
−0.015
−0.030
−0.045
0.009
0.006
0.003
0.000
−0.003
−0.006
−0.009

Figure.

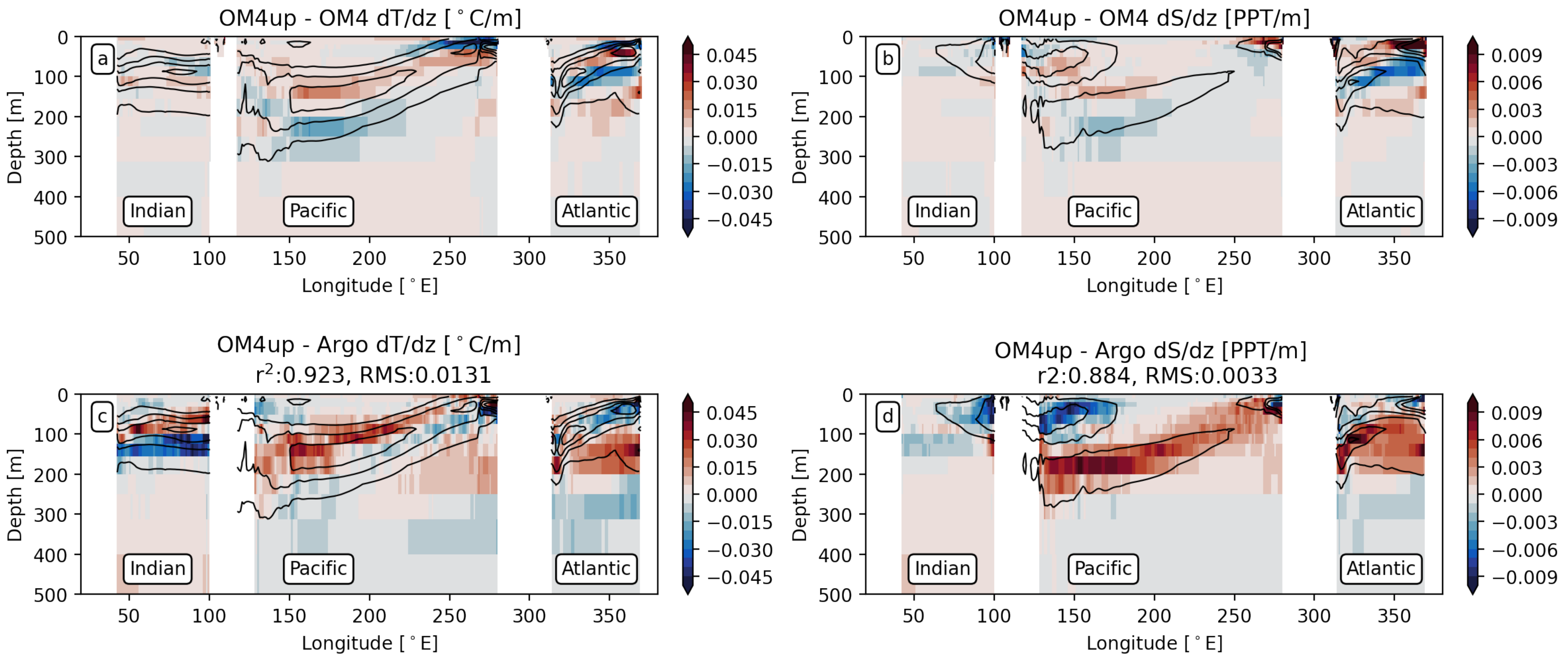

OM4up - OM4 dT/dz [$^\circ$C/m]
OM4up - OM4 dS/dz [PPT/m]
OM4up - Argo dT/dz [$^\circ$C/m]
r^2:0.923, RMS:0.0131
OM4up - Argo dS/dz [PPT/m]
r2:0.884, RMS:0.0033
a
b
c
d
Depth [m]
Longitude [$^\circ$E]
Indian
Pacific
Atlantic
0.045
0.030
0.015
0.000
−0.015
−0.030
−0.045
0.009
0.006
0.003
0.000
−0.003
−0.006
−0.009

Figure.

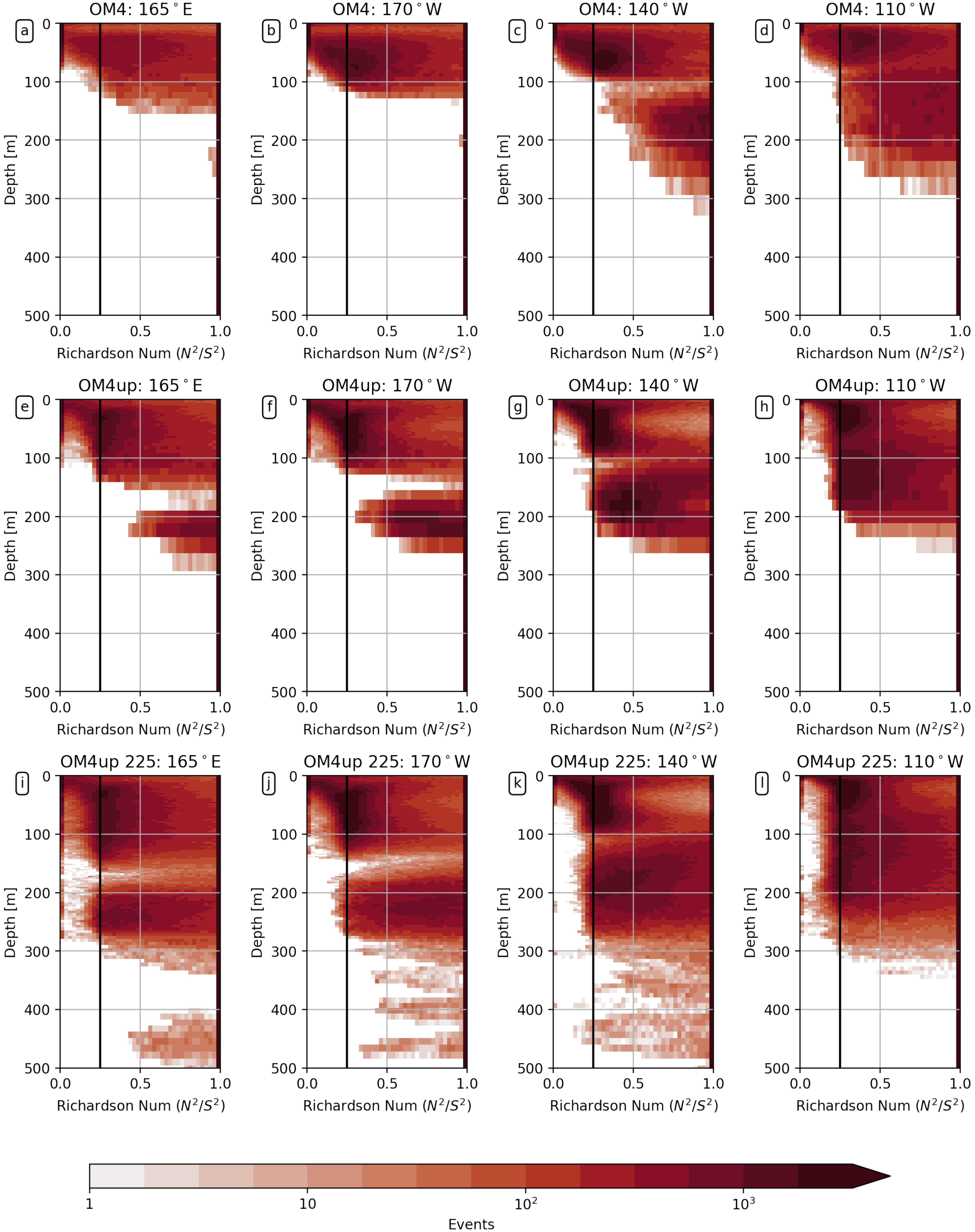

OM4: 165°E
OM4: 170°W
OM4: 140°W
OM4: 110°W
OM4up: 165°E
OM4up: 170°W
OM4up: 140°W
OM4up: 110°W
OM4up 225: 165°E
OM4up 225: 170°W
OM4up 225: 140°W
OM4up 225: 110°W
a
b
c
d
e
f
g
h
i
j
k
l
Depth [m]
Richardson Num (N^2/S^2)
Events
1
10
10^2
10^3

Figure.

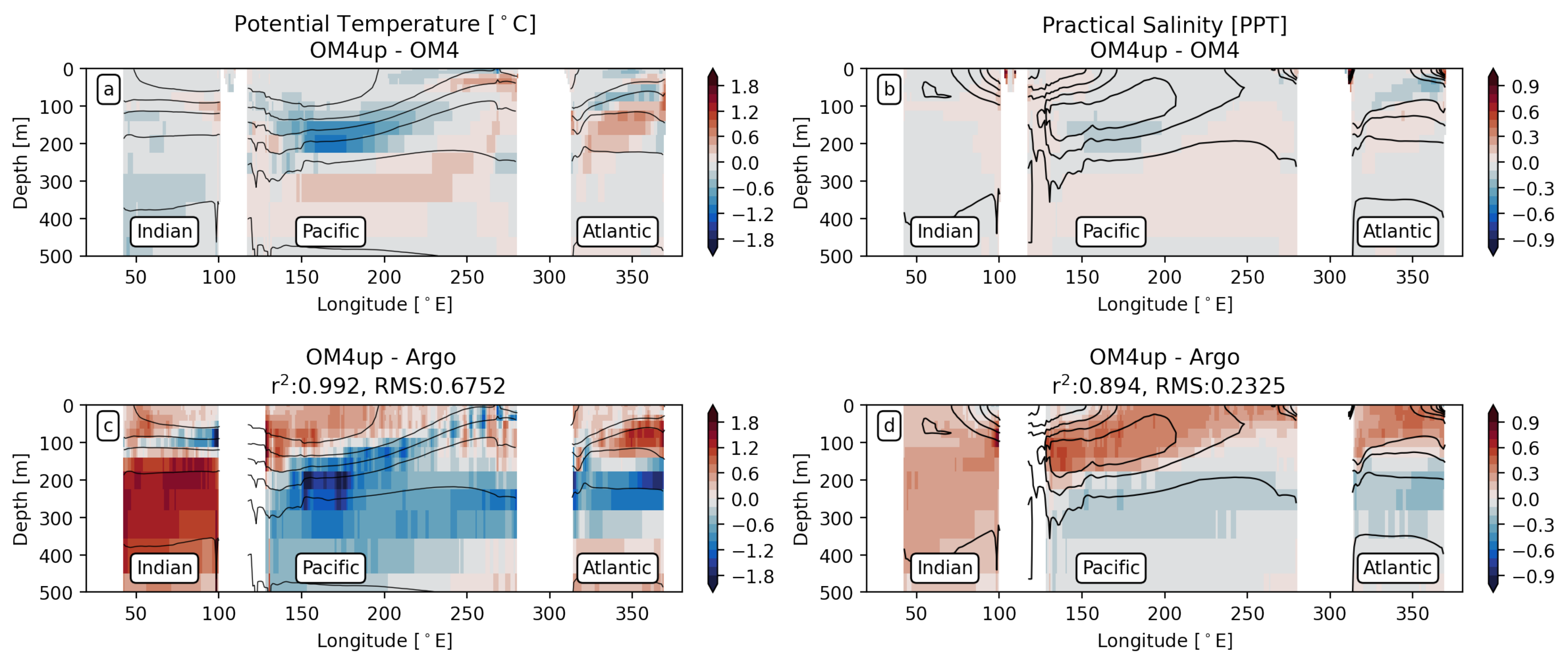
Potential Temperature [$^\circ$C]
OM4up - OM4
Practical Salinity [PPT]
OM4up - OM4
OM4up - Argo
r^2:0.992, RMS:0.6752
OM4up - Argo
r^2:0.894, RMS:0.2325
a
b
c
d
Indian
Pacific
Atlantic
Depth [m]
Longitude [$^\circ$E]
0
100
200
300
400
500
50
100
150
200
250
300
350
1.8
1.2
0.6
0.0
−0.6
−1.2
−1.8
0.9
0.6
0.3
0.0
−0.3
−0.6
−0.9

Figure.

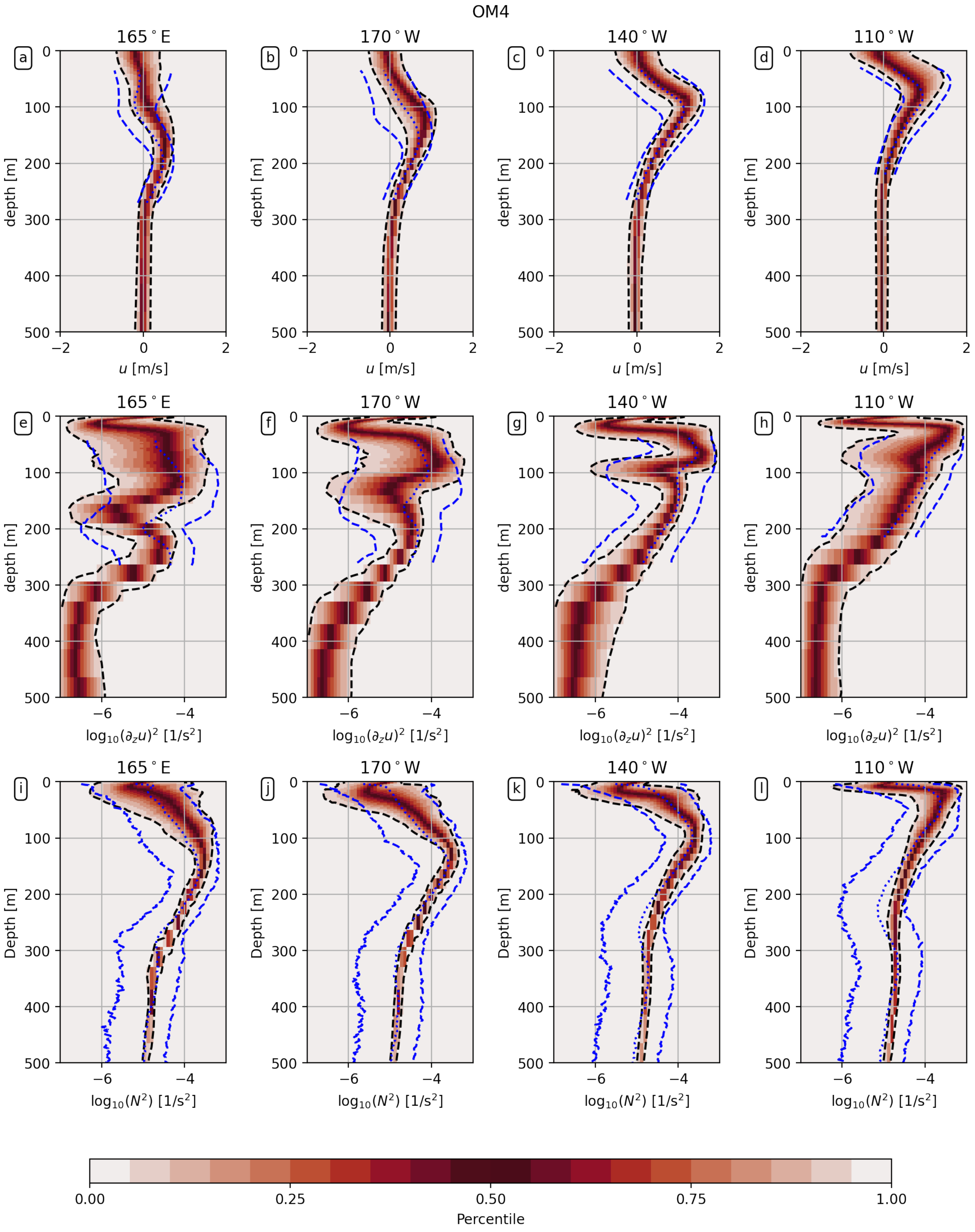

OM4
165°E
170°W
140°W
110°W
a
b
c
d
e
f
g
h
i
j
k
l
depth [m]
Depth [m]
u [m/s]
$\log_{10}(\partial_z u)^2$ [1/s^2]
$\log_{10}(N^2)$ [1/s^2]
Percentile
0.00
0.25
0.50
0.75
1.00

Figure.

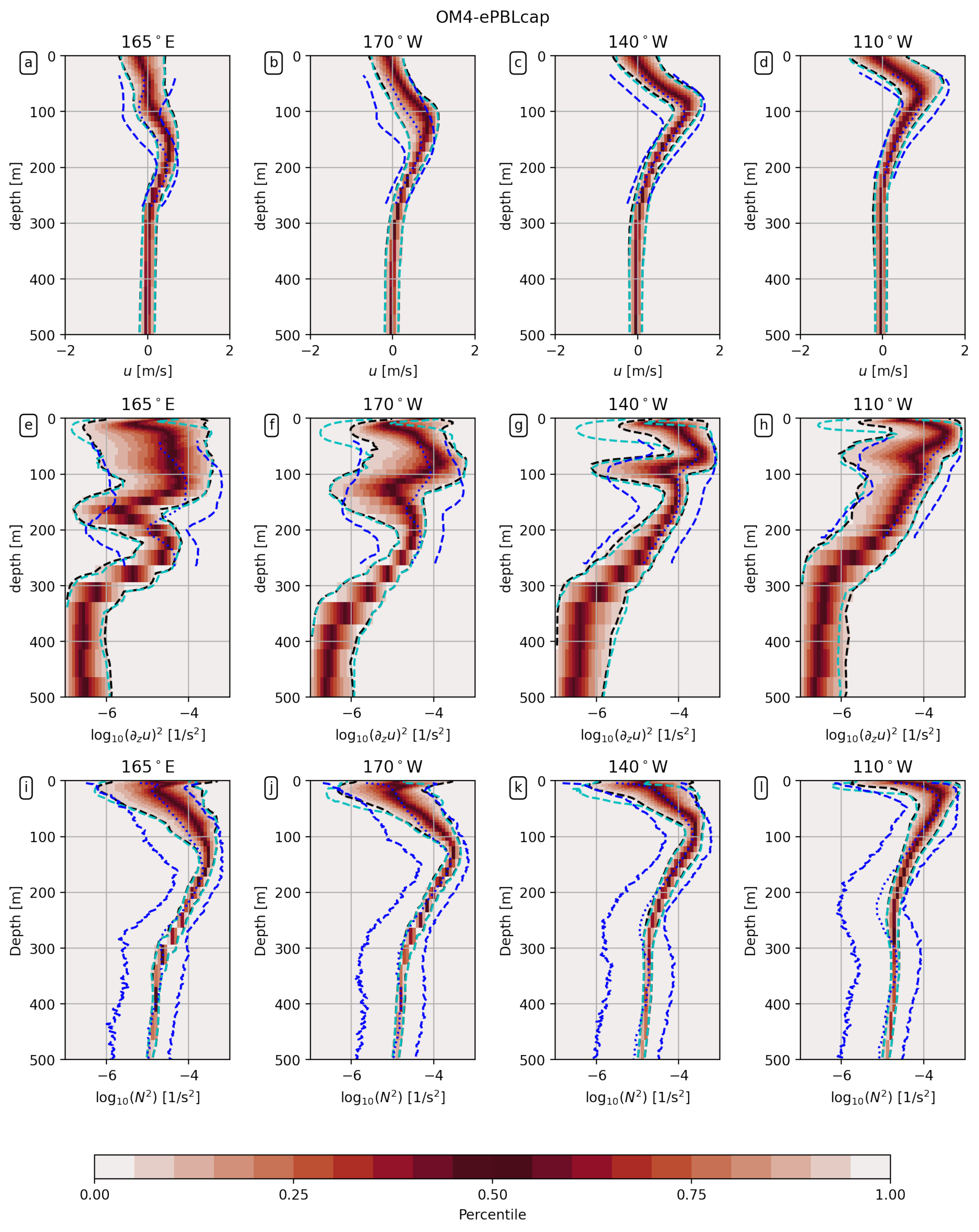
OM4-ePBLcap
165°E
170°W
140°W
110°W
a
b
c
d
e
f
g
h
i
j
k
l
depth [m]
Depth [m]
u [m/s]
log10(∂zu)^2 [1/s^2]
log10(N^2) [1/s^2]
Percentile
0.00
0.25
0.50
0.75
1.00

Figure.

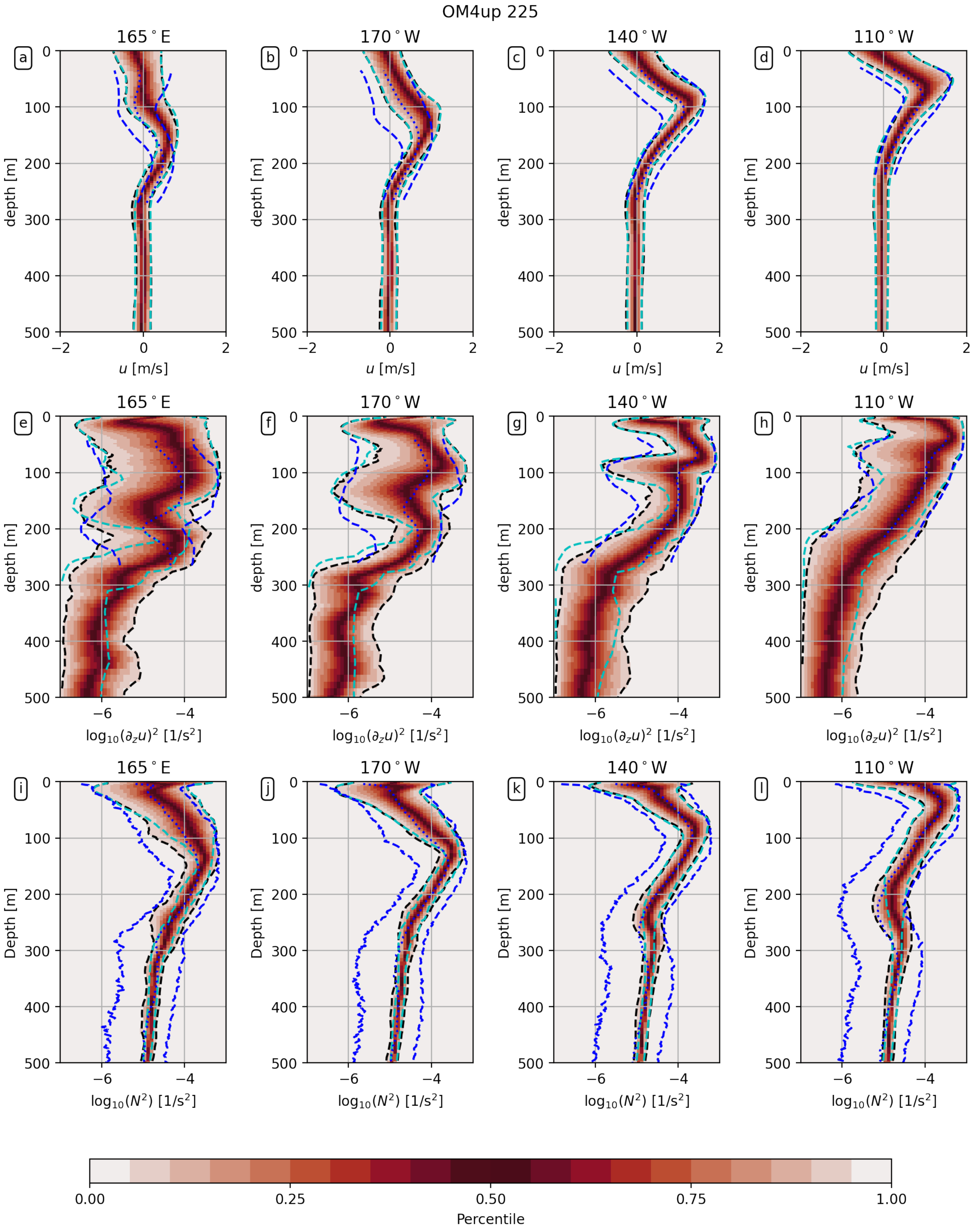
OM4up 225
165°E
170°W
140°W
110°W
a
b
c
d
e
f
g
h
i
j
k
l
depth [m]
Depth [m]
u [m/s]
$\log_{10}(\partial_z u)^2$ [1/s^2]
$\log_{10}(N^2)$ [1/s^2]
Percentile
0.00
0.25
0.50
0.75
1.00

Figure.

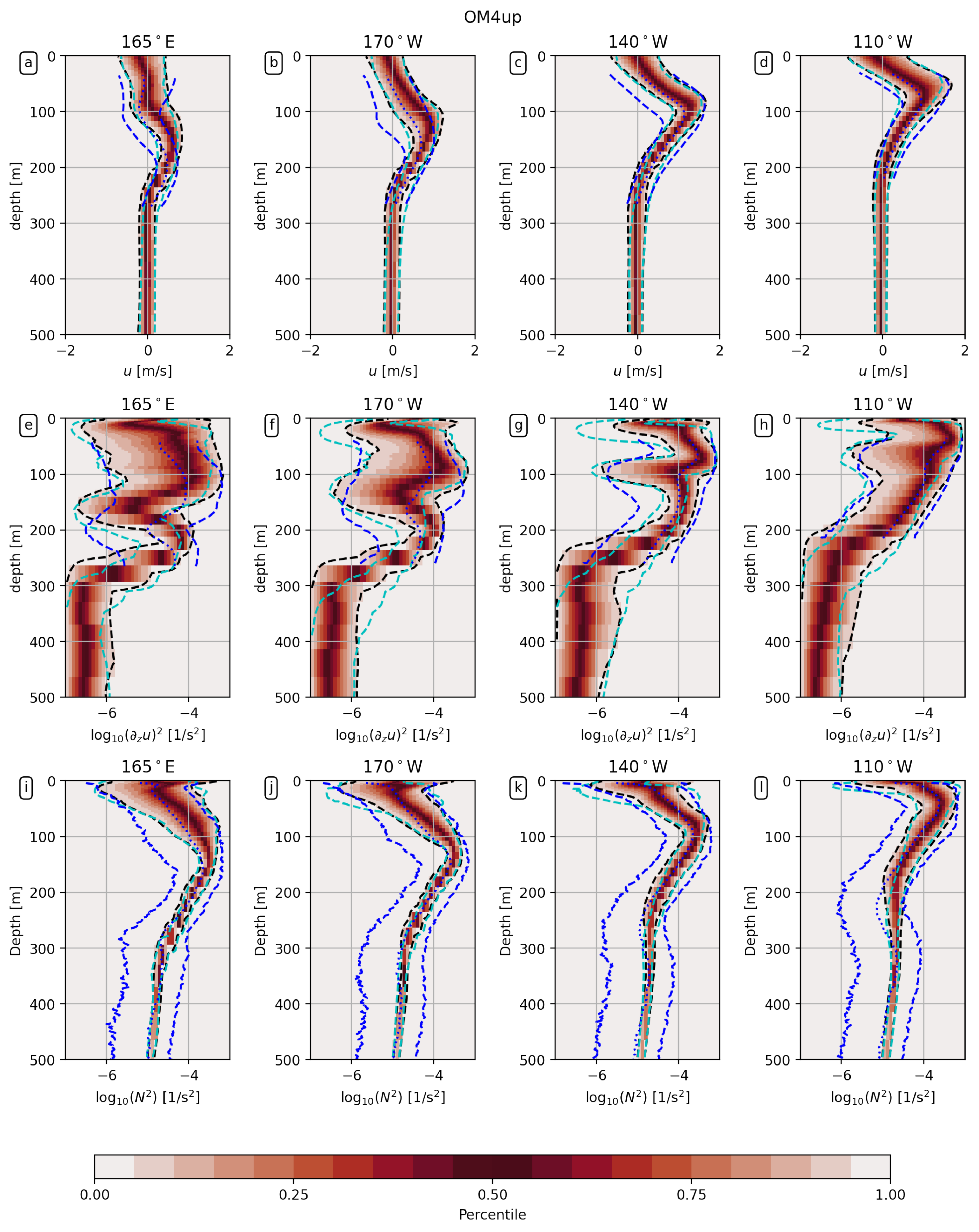
OM4up
165°E
170°W
140°W
110°W
a
b
c
d
e
f
g
h
i
j
k
l
depth [m]
Depth [m]
u [m/s]
log10(∂zu)^2 [1/s^2]
log10(N^2) [1/s^2]
Percentile
0.00
0.25
0.50
0.75
1.00

Figure.

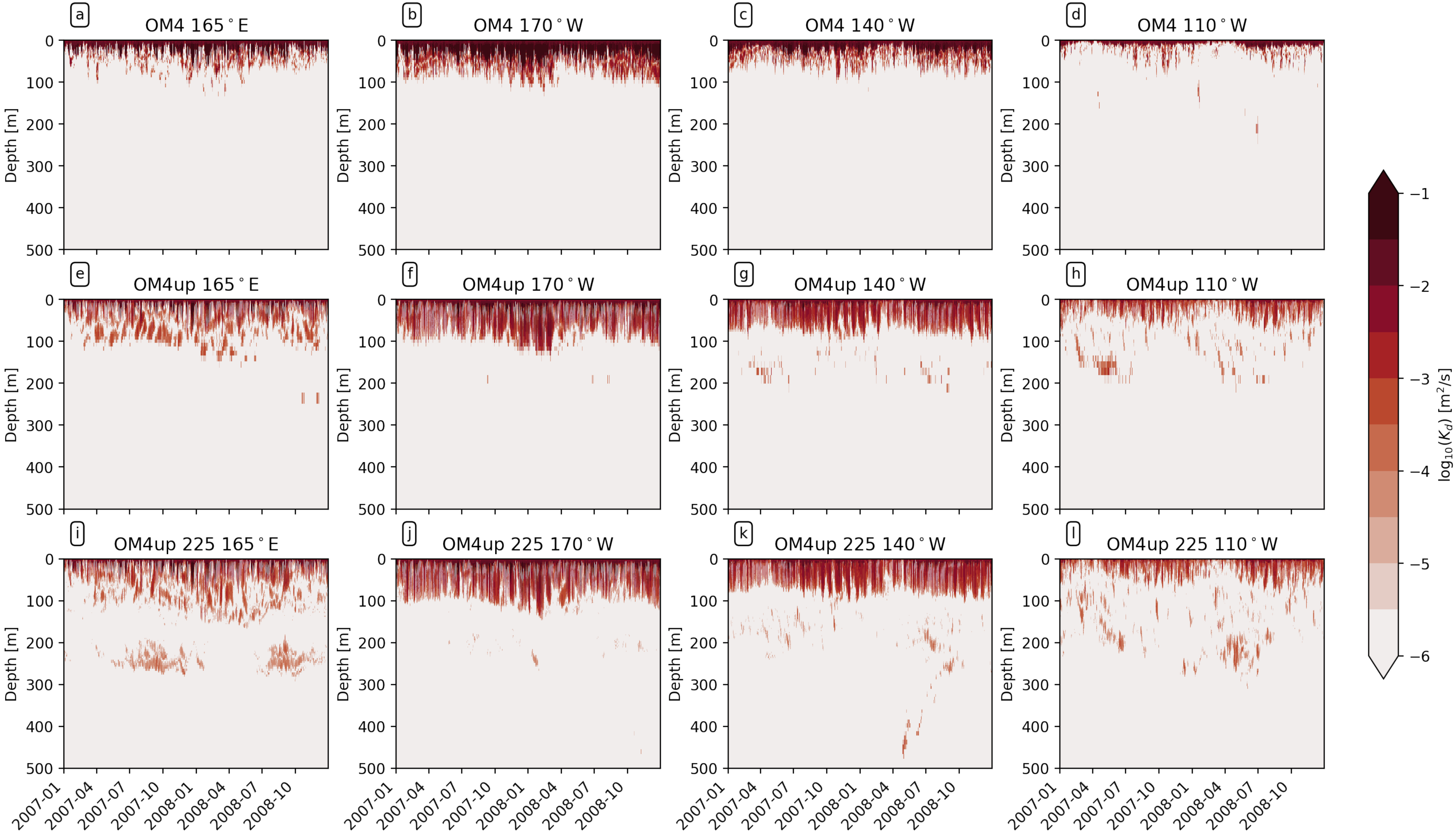

a
OM4 165°E
b
OM4 170°W
c
OM4 140°W
d
OM4 110°W
e
OM4up 165°E
f
OM4up 170°W
g
OM4up 140°W
h
OM4up 110°W
i
OM4up 225 165°E
j
OM4up 225 170°W
k
OM4up 225 140°W
l
OM4up 225 110°W
Depth [m]
0
100
200
300
400
500
2007-01
2007-04
2007-07
2007-10
2008-01
2008-04
2008-07
2008-10
log10(Kd) [m2/s]
−1
−2
−3
−4
−5
−6